Boundary-Layer Meteorology (2025) 191:5
https://doi.org/10.1007/s10546-024-00895-5

RESEARCH ARTICLE

# Surface Roughness in Stratified Turbulent Ekman Flow

**Jonathan Kostelecky**[1,2] · **Cedrick Ansorge**[1]

Received: 2 October 2024 / Accepted: 20 December 2024


**Abstract**
The interplay of surface roughness and stable stratification is investigated by direct numerical simulation of Ekman flow. Our setup is well within the turbulent regime, reaching a friction Reynolds number of $Re_\tau \approx 2700$. Further, we reach the verge of the fully rough regime under neutral conditions with a non-dimensional obstacle height $H^+ \approx 40$, corresponding to a z-nought parameter in viscous units $z_0^+ \approx 2$. Stability is imposed via a gradual decrease of surface buoyancy from neutral (no stratification) to very strong stratification. The reduced Reynolds number ($Re_\tau$) in comparison to atmospheric problems warrants consideration of viscous effects on our results, and we demonstrate a correction method that consistently incorporates viscous effects, thus reducing the spread of data from our numerical results. The weakly stable regime is maintained at higher stability due to efficient production of turbulence kinetic energy which counteracts buoyant restoring forces in the presence of roughness. When scaled according to Monin–Obukhov similarity theory (MOST) our results for weak stability compares excellent to known formulations based on atmospheric observations. The coefficients of the stability correction functions for momentum and heat are estimated as $\beta_\mathrm{m} = 3.45$, $\beta_\mathrm{h} = 5.21$ respectively, and we observe a slight but significant increase of the turbulent Prandtl number with stability. In the very stable regime, global flow properties (e.g. friction velocity, Obukhov length) oscillate with a decaying amplitude and global intermittency, i.e. the co-occurrence of turbulent/laminar fluid at large scale, is observed in the presence of roughness. In such very stable conditions, a strong veering of the surface wind with respect to the large-scale forcing ($< 90°$) is observed.

**Keywords** Boundary-layer turbulence · Direct numerical simulation · Monin–Obukhov similarity theory · Stable boundary layer · Surface roughness

## 1 Introduction

Static stability is ubiquitous in the atmospheric boundary layer (ABL) as radiative processes in vicinity of and at the underneath surface cause vertical temperature gradients at various time scales. In the mid-latitudes, the static stability primarily governs the ABL's diurnal cycle (cf. Figure 1.7 on p. 11, Stull 1988, ): During the day, the sun heats the Earth surface,

✉ Jonathan Kostelecky
j.kostelecky@posteo.de

[1] Institut für Meteorologie, Freie Universität Berlin, Carl-Heinrich-Becker-Weg 6-10, 12165 Berlin, Germany

[2] Institut für Geophysik und Meteorologie, Universität zu Köln, Pohligstr. 3, 50969 Cologne, Germany

plumes of warmer air rise from the ground, resulting in the well-mixed and turbulence-rich convective boundary layer. In absence of solar irradiation – during night or polar night – the surface cools and the stable boundary layer (SBL) forms, characterized by an upward increase of potential air temperature (Mahrt 2014).

Static stability makes the buoyancy conversion term a sink in the budget of turbulence kinetic energy (TKE), such that turbulence is exclusively generated by shear – a stark contrast to convective conditions where both buoyancy and shear generation are a source of TKE. The SBL is commonly classified according to the relative strength of stratification and the impact of stratification on turbulent transport and mixing. This gives rise to classification approaches, suggested, for instance, by Mahrt (1998); Howell and Sun (1999); Grachev et al. (2013); Stopa et al. (2022). Mahrt (1998) distinguishes the *weakly stratified* boundary layer (WSBL), where surface-layer similarity works very well, the temperature behaves like a passive scalar, and the interaction of stratification with the turbulence structure is weak, from the *very stable* boundary layer (VSBL), where buoyancy destruction of turbulence substantially changes the surface-layer flow. Windy conditions (when shear-generation of turbulence is strong), or moderate surface cooling give rise to the WSBL, characterized by a state of continuous turbulence at reduced intensity. For large surface-cooling or weak wind, in the VSBL, turbulence is suppressed, but a complete laminarization is not found in the atmospheric measurements for its high Reynolds number. In such intermittently turbulent flow (Businger 1973; Mahrt 1999; Ansorge and Mellado 2014; Shah and Bou-Zeid 2014; Deusebio et al. 2015) the upper part of the VSBL decouples from the surface layer.

The WSBL is amenable by Monin–Obukhov Similarity theory (MOST) for the atmospheric surface layer (ASL, Monin 1970; Högström 1988; Grachev et al. 2013) and by local similarity aloft (Nieuwstadt 1984). On the contrary, the VSBL is intricate and despite intense efforts over past decades, a number of issues remain unsolved (Holtslag et al. 2013; Sandu et al. 2013; Steeneveld 2014; LeMone et al. 2019; Edwards et al. 2020). Global intermittency plays a pivotal role in the VSBL, and it results in spatio-temporally complex organized turbulence, characterized by anisotropy and wave-like/non-turbulent interaction between laminar and turbulent flow (cf. gravity waves on p. 87, Businger 1973; Vercauteren et al. 2019; Van der Linden et al. 2020; Gucci et al. 2023, ). Most prominently, large-eddy simulation (LES) faces severe challenges in the VSBL for the locality, anisotropy, and inhomogeneity of turbulence (Jiménez and Cuxart 2005). A common problem is the local laminarization of the flow and the associated *runaway cooling* (Jiménez and Cuxart 2005; Van de Wiel et al. 2012a). These problems reflect a conceptual lack models of the VSBL and challenge classical modelling approaches, calling for new avenues in turbulence parameterization (e.g. Stiperski and Calaf 2018; Maroneze et al. 2023; Boyko and Vercauteren 2024, ). Here, we use direct numerical simulation (DNS) of the SBL to circumvent dependencies on turbulence closure models at the cost of (i) a simplified setup, (ii) high computational expense, and (iii) a reduced scale separation.

Neglecting the background rotation of the mean wind in the ASL, which is in accordance with MOST, the ASL can be studied by virtue of the channel-flow analogy. DNS of stratified channel flow (Garg et al. 2000; Nieuwstadt 2005; Flores and Riley 2011; García-Villalba and del Álamo 2011; Donda et al. 2015, 2016, among others), commonly focuses on the collapse of turbulence and associated laminarization in the intermittently turbulent regime. The Obukhov length scaled in viscous units (later defined as $L_O^+$ and sometimes termed buoyancy Reynolds number) for its appropriate characterization of turbulence instability in a stratified flow–is identified as relevant scaling parameter for the turbulence collapse (Flores and Riley 2011). Over a smooth surface, the flow laminarizes below $L_O^+ \approx 100$. For heterogeneous surface conditions, they speculate $L_O/L_R$, where $L_R$ is a characteristic roughness length scale,

is the appropriate parameter. This would suggest that roughness shifts the stability threshold for transition to a laminar or intermittently turbulent flow to higher stability. More recently, Mironov and Sullivan (2023) investigate the turbulence structure in a stratified Couette flow for a thermally heterogeneous bottom boundary. They indeed demonstrate maintenance of turbulence in very stable conditions over thermally heterogeneous surfaces due to the presence of local convective instability as a consequence of the thermal heterogeneity.

When the ABL is considered in its vertical entirety, Earth rotation, i.e. the Coriolis force, manifests in a wind veer. This veer gives rise to the Ekman spiral (Ekman 1905) and a loss of the lateral (spanwise) flow symmetry in comparison with channel flow. Rotational effects are adequately represented in Ekman flow, the flow over a flat, rotating plate. The boundary layer depth scale (outer scale) of the Ekman flow $\delta = u_\tau / f$, with the friction velocity $u_\tau$ and the Coriolis parameter $f$, is constant under neutral stratification, but unknown *a priori* to the simulation. The total turbulent scale separation of the outer $\delta$ (largest eddies of the size of the boundary layer scale) and inner scale $\delta_\nu$ (smallest eddy size, where dissipation becomes relevant) of the flow problem is expressed as the friction Reynolds number $Re_\tau$, defined as:

$$Re_\tau = \frac{\delta}{\delta_\nu} = \frac{u_\tau \delta}{\nu}, \tag{1}$$

where $\delta_\nu$ is the viscous unit and $\nu$ the kinematic viscosity.

The neutrally stratified problem was studied by Coleman et al. (1990); Coleman (1999); Shingai and Kawamura (2004); Miyashita et al. (2006); Spalart et al. (2008, 2009); Marlatt et al. (2012); Ansorge (2019). Different regimes of density stratification are explored in Coleman et al. (1992); Ansorge and Mellado (2014, 2016); Shah and Bou-Zeid (2014); Deusebio et al. (2014); Stefanello et al. (2022). The turning angle of the wind increases with stability, while a drastic decrease of the boundary layer height is observed. The studies by Ansorge and Mellado (2014, 2016) enabled a qualitative representation of the turbulence regimes only by varying the strength of stability, measured by an external bulk Richardson number. At sufficient stability, global intermittency is intrinsic to the VSBL and does not require external trigger mechanisms. This intermittency occurs in space and time rather than as an on–off processes in time which calls for conditional analysis and at the same time emphasizes the importance of the laminar patches in the flow's surface layer. As previous studies have indicated, DNS of very stable Ekman flow with global intermittency are demanding for various reasons: (i) the scale separation in terms of the friction Reynolds number $Re_\tau$ has to be large enough, (ii) fine grid resolution is necessary to resolve the occurrence of large gradients in turbulent patches, (iii) large domain sizes are required to accommodate large-scale flow structures and laminar/turbulent patches.

The aforementioned studies of Ekman flow cover a broad range of stratification, but they are mainly constrained to aerodynamically smooth surfaces. At the same time, surface roughness is an omnipresent and multiscale feature in the ABL. More importantly, the effect of roughness is pronounced in the SBL, since the ABL thickness decreases by up to an order of magnitude in contrast to neutral stratification, from $\mathcal{O}(1\ km)$ to $\mathcal{O}(10-100\ m)$ (cf. semi-empirical boundary layer depth scheme for neutral and stable stratification by Zilitinkevich et al. 2012, based on LES and observational data). An exception is Lee et al. (2020), who study stratified Ekman flow over a periodic cosine-shaped hill. Their roughness setup is located in the transitionally rough regime with $H^+ = 15$, where $H^+$ is the height $H$ of the bumps expressed in viscous units. A regime shift from the VSBL to the WSBL is observed, since roughness is a triggering mechanism of turbulence and therefore counteracts the stability-induced suppression of turbulence. More recently, Bhimireddy et al. (2024) describe the effect of roughness on the SBL based on tower measurement from field observations and find

that the increase in the turbulent velocity scale $V_{TKE}$ (equal to the square root of the TKE) with the wind speed increases with the roughness length.

In a preliminary study (Kostelecky and Ansorge 2024a, hereafter KA24), we investigated the effect of small-scale surface roughness on bulk properties of the neutrally stratified ABL—based on first principles, i.e. using DNS. The cases in KA24 only differ with respect to the mean height of the roughness, and they cover the transitionally rough regime up to the verge of the fully rough regime. From the DNS perspective, the setup exhibits a relatively large scale separation in terms of the friction Reynolds number $Re_\tau$ (up to $Re_\tau \approx 2700$). In fact, this scale separation is sufficient to explore the rough-wall scaling of the logarithmic layer for velocity and a passive scalar, which allows extrapolation of our results to the high-Reynolds-number regime in which the ABL is generally found. Here, we extend the setup introduced by KA24 to stable stratification, and investigate four research questions: (1) Does the presence of roughness extend the stability regime in which turbulence is maintained, and how is the regime transition from weak to very stable s roughness? (2) Does large-scale intermittency occur in the very stable regime and are its effects comparable to those in aerodynamically smooth flow? (3) How does the flow topology change? (4) Are common stability corrections for MOST applicable to our data and do the associated values of the von Kármán constant $\kappa$, aerodynamic roughness length $z_0$ and the zero-plane displacement height $d$ match expectations based on observational data from atmospheric measurement campaigns?

## 2 Methodology

We approach the problem by DNS. The governing equations and their non-dimensionalization are described in Sect. 2.1 followed by the algorithm used to solve the equations (Sect. 2.3). The treatment of a rough surface and introduction of stable density stratification are described in Sect. 2.4 and Sect. 2.5 before we introduce the set of simulation cases in Sect. 2.6.

### 2.1 Governing Equations

We solve the incompressible Navier–Stokes equations numerically under the Boussinesq approximation in a horizontally doubly-periodic domain. Stratification effects are represented by buoyancy:

$$b = \frac{\theta'}{\theta_0} g_{\text{grav}}, \tag{2}$$

with the gravitational acceleration $-g_{\text{grav}}\hat{e}_3$ (pointing downwards). Neglecting diabatic heating, the energy conservation equation then becomes an advection–diffusion equation for buoyancy. Here, $\theta_0$ is a reference temperature throughout the domain and $\theta'$ is the local deviation from this temperature. For non-dimensionalization of the system, we use the geostrophic wind $G$ (with $\mathbf{G} = (G_1, G_2, 0)^T$, and $G = \sqrt{G_1^2 + G_2^2}$), the Rossby radius $\Lambda_{Ro} = G/f$ with the Coriolis parameter $f$, and the buoyancy difference $\Delta B = B_0 - 0$ between the bottom and top boundaries of the domain. With these scales, the non-dimensionalized governing equations for continuity, momentum and buoyancy become (hats over dimensionless variables are dropped for convenience):

$$\frac{\partial u_i}{\partial x_i} = 0, \tag{3a}$$

$$\frac{\partial u_i}{\partial t} + u_j \frac{\partial u_i}{\partial x_j} = -\frac{\partial \pi}{\partial x_i} + \frac{1}{Re_\Lambda} \frac{\partial^2 u_i}{\partial x_j^2} + \epsilon_{ik3}(u_k - g_k) + Ri_\Lambda b \delta_{i3}, \tag{3b}$$

$$\frac{\partial b}{\partial t} + u_j \frac{\partial b}{\partial x_j} = \frac{1}{Re_\Lambda Pr} \frac{\partial^2 b}{\partial x_j^2}, \tag{3c}$$

with boundary conditions corresponding to Ekman flow:

$$\begin{pmatrix} u_i|_{z=0} \\ u_i|_{z=z_{\text{top}}} \end{pmatrix} = \begin{pmatrix} 0 \\ g_i \end{pmatrix} \quad \text{and,} \tag{3d}$$

$$\begin{pmatrix} b|_{z=0} \\ b|_{z=z_{\text{top}}} \end{pmatrix} = \begin{pmatrix} 0 \\ B_0 \end{pmatrix}. \tag{3e}$$

Here, $t$ is the time, $x_i$ the Cartesian coordinates with $x_i = (x, y, z)^T$, where $x, y$ are the streamwise, spanwise directions and $z$ the wall-normal coordinate (pointing upwards from the ground). The corresponding velocity vector is $\mathbf{u} = (u, v, w)^T = (u_1, u_2, u_3)^T$. The ageostrophic non-hydrostatic pressure is $\pi$ and the non-dimensional geostrophic wind vector is $\mathbf{g} = (g_1, g_2, 0)$.

In case of $Ri_\Lambda = 0$ (no buoyancy), the buoyancy equation (3c) reduces to an equation for a passive scalar $s$ (non-dimensionalized with $\Delta S$, the scalar difference between bottom and top boundaries), without feedback on the momentum equations, since the buoyancy term in (3b) is dropped.

### 2.2 Dimensionless Parameters

The system of Eqs. (3a–3c) is governed by three dimensionless parameters,

$$Re_\Lambda = \frac{G \Lambda_{Ro}}{\nu}, \tag{4a}$$

$$Pr = \frac{\nu}{\kappa_d}, \tag{4b}$$

$$Ri_\Lambda = \frac{\Delta B \Lambda_{Ro}}{G^2}, \tag{4c}$$

the external Reynolds number $Re_\Lambda$, the molecular Prandtl number $Pr$ and the bulk Richardson number $Ri_\Lambda$ with the constant kinematic fluid viscosity $\nu$ and constant molecular diffusivity $\kappa_d$. The Reynolds number $Re_D = GD/\nu = \sqrt{2Re_\Lambda}$, the Richardson number $Ri_D = \Delta B D/G^2 = Fr^{-2}$ ($Fr$ being the Froude number), based on the laminar thickness of the Ekman layer $D = \sqrt{2\nu/f}$ and the Richardson bulk number $Ri_B = \Delta B \delta_N / G^2$, with the turbulent boundary thickness $\delta_N$ for a neutral flow, are given for comparison with other studies. Whereas the ratios of $Re_D/Re_\Lambda$ and $Ri_D/Ri_\Lambda$ reduce to the length scale ratio of the system of $D/\Lambda_{Ro}$.

The study of the turbulent problem requires a mapping from the non-dimensionalization with external parameters to the classical inner $(\cdot)^+$ and outer $(\cdot)^-$ normalization for velocities and length scales (KA24):

$$x_i^+ = x_i u_\star Re_\Lambda, \tag{5a}$$

$$u_i^+ = \frac{u_i}{u_\star}, \tag{5b}$$

$$x_i^- = \frac{x_i}{u_\star}, \tag{5c}$$

$$u_i^- = u_i. \tag{5d}$$

The inner and outer scales are mapped by $x_i^+ = Re_\tau x_i^-$ and $u_i^- = u_\star u_i^+$. Here, $x_i^+ = x_i \Lambda_{Ro} u_\tau / \nu$, with the dimensional coordinate $x_i \Lambda_{Ro}$ and the viscous unit $\nu/u_\tau$. The non-dimensional friction velocity $u_\star = u_\tau / G$, where $u_\tau$ is corresponding dimensional quantity and is derived from an integration procedure described in KA24, which is linked to the non-dimensional boundary layer depth scale $\delta_{\star N} = u_{\tau N} (\Lambda_{Ro} f)^{-1} = u_{\star N}$ for neutral conditions (subscript $(\cdot)_N$). Further, we define the non-dimensional boundary layer depth scale $\delta_{\star,95}$ (cf. their Eq. 30, here without extrapolation, Kosović and Curry 2000), of relevance for stable stratification, defined as:

$$\delta_{\star,95} = z \left( \frac{\sqrt{\langle u'w' \rangle^2 + \langle v'w' \rangle^2}}{u_\star^2} = 0.05 \right), \tag{6}$$

the height, where the total vertical momentum stress is 5 % of the total stress. In the following, the temporal averaging of the flow variables is denoted by $\overline{(\cdot)}$ and spatial averaging in the horizontal by $\langle (\cdot) \rangle$.

In stratified flow, the Obukhov length $L_O$ (Obukhov 1971; Nieuwstadt 2005; Flores and Riley 2011) is commonly used to describe the relative impact of stratification. Here, for the choice of Dirichlet boundary conditions for buoyancy, the evolution of $L_O$ is part of the solution, i.e. unknown *a priori*. As such we diagnose it from the simulations. When expressed in viscous units, $L_O^+ = Re_L$ is a Reynolds number, sometimes termed the buoyancy Reynolds number, and it can be interpreted as the inverse of the gradient-Richardson number $Ri_G$ evaluated at the surface (Ansorge and Mellado 2014) (commensurate with a flux-Richardson number $Ri_F$ evaluated at the bottom of the constant flux layer):

$$L_O^+ = L_O \frac{u_\tau}{\nu} = \left( \frac{u_\star^3}{u_\star b_\star} \right)^+, \tag{7a}$$

$$Ri_G = \frac{1}{L_O^+}. \tag{7b}$$

The buoyancy friction value $b_\star$ is derived with an integration procedure described in KA24 (similar procedure to $s_\star$, the friction value of the passive scalar). In contrast to Obukhov (1971), we follow the definition of Nieuwstadt (2005) and skip the von Kármán constant $\kappa$. Therefore, the mapping is according to $L_O^{O71} = \kappa^{-1} L_O$, where $L_O^{O71}$ is the Obukhov length including the von Kármán constant as introduced by Obukhov (1971).

### 2.3 Algorithm

For the simulation and analysis of turbulent flow we use the highly scalable and MPI-parallel tool-suite `tLab`,[1] which is open-source and contains an extensive documentation, validation routines and examples. `tLab` is based on a factorization of the pressure-Poisson equation, as

[1] https://github.com/turbulencia/tlab.

discussed by Mellado and Ansorge (2012), where details on the numerics and validation of the code can be found. The horizontally periodic flow problem is discretized and solved in a finite-size cuboidal domain $[L_x, L_y, L_z]$ using compact Padé schemes of sixth order in the interior of the domain (Lele 1992) and a fourth-order five-stage low-storage Runge–Kutta scheme (Williamson 1980).

### 2.4 Surface Roughness

Roughness is represented via an immersed boundary method (IBM). Here, we use the alternating direction reconstruction IBM (ADR IBM, based on Giannenas and Laizet 2021) with cubic splines to fully resolve obstacles in the flow. The implementation of the ADR IBM in the DNS code is discussed in Sect. 2.4 in KA24.

As roughness setup in the whole study we choose the case `r3` (cf. KA24, Fig. 3), with $56^2$ square blocks located at the lower domain boundary. To introduce a certain degree of randomness, the blocks are slightly displaced from a regular grid and heights, widths of the elements are uniformly distributed within $\Delta H^+ = 13.8$, $\Delta W^+ = 27.6$ and therefore:

$$H \in \left[ H^+ - \frac{\Delta H^+}{2}, H^+ + \frac{\Delta H^+}{2} \right], \tag{8a}$$

$$W \in \left[ W^+ - \frac{\Delta W^+}{2}, W^+ + \frac{\Delta W^+}{2} \right]. \tag{8b}$$

The mean height is $H^+ = 40.8$ and the mean width is $W^+ = 55.2$. The roughness morphology is characterized by the plan area density of $\lambda_p = A_P/A_T \approx 10\%$ and frontal solidity of $\lambda_f = A_F/A_T \approx 7\%$, with the total surface area $A_T$, the frontal area $A_F$ and the plan area $A_P$ occupied by all roughness elements (cf. Figure 2 in Grimmond and Oke 1999, ). This particular choice is considered as small-scale surface roughness, since the scale separation measured in $Re_\tau = 2688$ is large from the DNS perspective and thus results in a small blocking ratio of $H/\delta \approx 1.5\%$ for relevance of the ABL. Case `r3` is on the verge of the transition to the fully rough regime, with a diagnosed apparent roughness length of $z_{0\mathrm{m}}^+ \approx 2$. This roughness setup is at the limit of what is possible with the available computational resources.

### 2.5 Stratification

For progression to the regimes of stronger stability, we use a constant-in-time Dirichlet boundary condition for the buoyancy (Eq. 3e). This allows us to analyze the quasi-steady state that is reached once the SBL is in equilibrium with the stratification imposed. Provided the perturbation is not too large, the expected duration for this equilibrium to be reached is on the order of the eddy-turnover time $f^{-1}$. (Where the eddy-turnover time emerges as the ratio of the boundary layer depth scale and the turbulent velocity scale.) For the first stratified case, which is well within the weakly stratified regime, we use the flow fields from the neutrally stratified precursor simulations as initial condition in combination with the initial temperature profile described in Fig. 1, where the entire gradient is located above the highest roughness elements, since mixing is strong here.

The subsequent cases with higher stratification use the turbulent fields of buoyancy and momentum from its respective precursors as initial condition (vertical connections in Fig. 2). The increase in stratification is represented by a change in the Richardson number, which corresponds to a ramp-up in stratification across the boundary layer. The presence of realistic

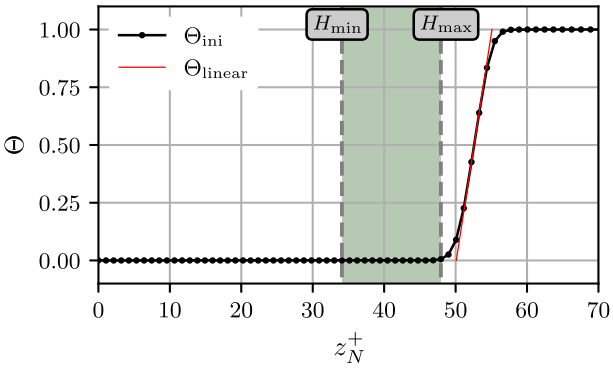


**Fig. 1** Temperature profile used for initialization of the first stratified case `S001` in black. The linear temperature profile (gradient corresponding to $L_O^+ \approx 1000$) in red is smoothed to the boundary values. The gradient is concentrated at the highest roughness elements $z_N^+ > H_{\max}$ (green shaded area relates to the range of roughness element heights). The subscript $(\cdot)_N$, relates to the viscous units of the neutral case. The numerical values of $\Theta_{\text{ini}}$ can be found in the available data in Kostelecky and Ansorge (2024b) (10.17169/refubium-45292)

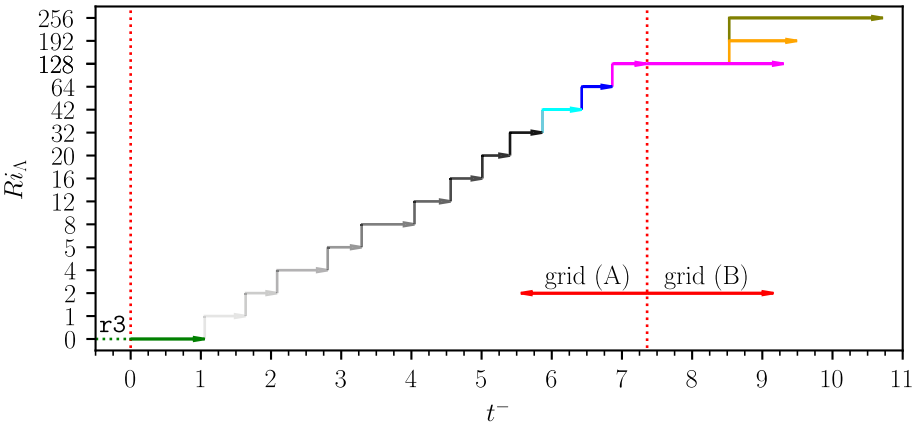


**Fig. 2** Temporal evolution of $Ri_\Lambda$ for the sequence of stratified simulation (cf. Table 2). The neutral precursor simulation `r3` is shown as a green arrow ($t^- > 0$) and dashed line ($t^- < 0$). Further, the computational grid is changed in favour of a lower one to resolve less of the laminar fluid aloft the PBL from (A) to (B) at $t^- \approx 7.3$, where $t^-$ is the eddy turnover time $f^{-1}$

turbulent perturbations in the initial fields (i) avoids a potential complete laminarization of the flow, which leads on the one hand in a slow recovery and on the other to strong turbulent bursts, which are numerically challenging (large gradients), and (ii) is a viable approach to present the build-up of stable density stratification following the evening transition. At the same time, however, each case reaches a quasi-steady state that can be analyzed in accordance with surface-layer similarity. The aim of this procedure is not to exactly mimic a realistic transition of the boundary layer but to enable a fast transition of the simulations into the quasi-steady state where we can analyze the data in accordance with surface-layer similarity.

**Table 1** (a) Dimensionless numbers, grid and domain parameters for all cases

| $Re_\Lambda$ | $Re_D$ | $Pr$ | $N_{xy} \times N_z$ | $(L_{xy} \times L_z)/\delta_N^3$ | $\Delta xy_N^+ \times \Delta z_{N,\min}^+$ |
|---|---|---|---|---|---|
| $5{\cdot}10^5$ | $10^3$ | 1.0 | $3840^2 \times 704$ (A) | $3.7^2 \times 3.5$ (A) | $2.6^2 \times 1.0$ |
| | | | $3840^2 \times 576$ (B) | $3.7^2 \times 1.5$ (B) | |

Grids (A) and (B) are used in this study, with the latter (B) being cropped from the top. The domain size normalized with the Rossby radius is (A) $(L_{xy} \times L_z)/\Lambda_{Ro}^3 = 0.27^2 \times 0.26$ and (B) $(L_{xy} \times L_z)/\Lambda_{Ro}^3 = 0.27^2 \times 0.11$

### 2.6 Simulations

Tables 1 and 2 list the simulations used here. All cases share the same heterogeneity pattern corresponding to case `r3` in KA24, consisting of $56 \times 56$ roughness elements in quasi-random arrangement. The molecular Prandtl number is $Pr = 1$, and the external Reynolds is fixed at $Re_\Lambda = 5 \cdot 10^5$, corresponding to $Re_D = 1000$. As initial condition, we use three-dimensional fields of momentum and buoyancy of case `r3` in KA24. These data reside on a grid of $N_{xy} \times N_z = 3072^2 \times 656$ collocation points and are interpolated to grid (A) (cf. Table 1), i.e. a slightly increased resolution. This is necessary as stronger gradients in stratified flow (causing higher velocities in vicinity of roughness elements) pose numerical challenges at the vertical walls of roughness elements. As a consequence of interpolating the fields, the surface roughness of case `N` is not identical with case `r3`, but it features identical statistical properties (mean height, width and distributions). Case `N` is run without stratification to equilibrate the new roughness configuration on grid (A) before stratification is added to the problem.

Starting from the neutral case `N`, stratification is sequentially increased in 12 steps from the weak to the very strong stability (cf. Table 2 and Fig. 2). In the very stable regime, three cases (`S128P, S192P, S256P`) are run in parallel on the new grid (B). Grid (B) is similar to (A) but cropped on top to decrease computational cost, since the boundary layer thickness is substantially decreased compared to the weakly stable cases.

Numerical integration is accomplished with the algorithm suite `tLab` on the high-performance computing system `hawk` at HLRS Stuttgart. Simulations were run for 86.5 days of wall-clock time on 128 nodes (16,384 physical CPUs). The total simulation period covers a time span $\Delta t_{\text{total}}^- = \sum_{i=1}^{N=16} \Delta t_{\text{sim,i}}^- = 12.37$, which corresponds to one week of wall-clock time or 21, 500 Node-hours per eddy turnover period $(1/f)$. Processed results are available for download in Kostelecky and Ansorge (2024b) (doi:10.17169/refubium-45292).

## 3 Bulk Statistics and Turbulence Regimes

### 3.1 Surface Friction and Boundary-Layer Depth

We commence by analyzing the statistics that form once the boundary layer has reached a quasi-steady state in equilibrium with the surface state. Each increment in stratification, viz. $Ri_\Lambda$, is followed by an adaptation period on the order of an eddy-turnover time (this initial transient is depicted by dotted lines in Figs. 3, 5). During this initial transient, surface-layer similarity is not expected to hold, and it is consequently excluded from subsequent analysis.

**Table 2** Overview of the simulation cases of this study, with the corresponding stratification level (Richardson numbers), grid type and the total simulation time in eddy-turnover times $f^{-1}$ for each case

| Case (ID) | $Ri_\Lambda$ | $Ri_B$ | Grid | $\Delta t^-_{\mathrm{sim}}[1/f]$ | (ID) |
|---|---|---|---|---|---|
| N | 0 | 0.000 | A | 1.06 | |
| S001 | 1 | 0.073 | A | 0.58 | |
| S002 | 2 | 0.147 | A | 0.44 | |
| S004 | 4 | 0.293 | A | 0.71 | |
| S005 | 5 | 0.367 | A | 0.48 | |
| S008 | 8 | 0.587 | A | 0.74 | |
| S012 | 12 | 0.880 | A | 0.51 | |
| S016 | 16 | 1.174 | A | 0.44 | |
| S020 | 20 | 1.467 | A | 0.39 | |
| S032 | 32 | 2.348 | A | 0.45 | |
| S042 | 42 | 3.081 | A | 0.55 | |
| S064 | 64 | 4.695 | A | 0.43 | |
| S128 | 128 | 9.390 | A | 0.48 | |
| S128P | 128 | 9.390 | B | 1.95 | |
| S192P | 192 | 14.086 | B | 0.97 | |
| S256P | 256 | 18.781 | B | 2.19 | |

Notation of case ID: N for neutral, S for stable, P for concurrent runs and numbering according to the value of $Ri_\Lambda$

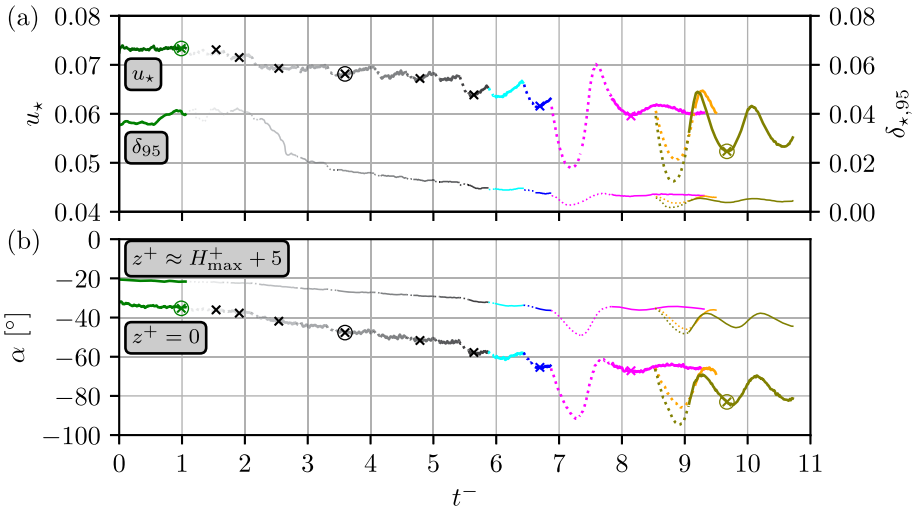


**Fig. 3** **a** Temporal evolution of the friction velocity $u_\star(t^-)$ (thick lines) and boundary layer thickness $\delta_{\star,95}(t^-)$ (6, thin lines). **b** Wind veer $\alpha(t^-)$ at the surface $z^+ = 0$ (thick lines) and above the roughness elements $z^+ \approx H^+_{\mathrm{max}} + 5$ (thin lines). Markers for the analysis in Sect. 3.5. The coordinate system is aligned with the geostrophic wind for estimating the wind veer. Dotted lines are excluded from the analysis, since these parts are identified as initial transients. Case S128 ($6.8 \leq t^- \leq 7.8$) is out of equilibrium and therefore excluded from subsequent analysis

If stratification is weak, the buoyancy term in the momentum equations is small in comparison to the dominant balance in the ASL. In such conditions, the downward buoyancy flux is limited by small temperature gradients, and no substantial changes in the bulk statistics (Fig. 3) are found. This is the case for our simulations S001–S002 ($t^- \leq 2.1$) where buoyancy acts as a passive scalar. From case S004 onward, buoyancy starts o act on the flow fields, and the thickness of the boundary layer, measured in terms of $\delta_{\star,95}$, decreases by about 50 % (Fig. 3a). With increasing stratification, $\delta_{\star,95}$ decreases to approximately one fifth of its neutral value for case S064 ($5.8 \leq t^- \leq 6.8$). In contrast, the friction velocity decreases only slightly so that the ratio $\delta_{\star,95}/\delta_\star$ (not shown) drops from its neutral value $0.5 - 0.6$ to approximately 0.1 for the most stable cases. This indicates that shear production ($u_\star$) is no longer the single appropriate scaling variable in the surface layer. Indeed, the Obukhov length $L_O$, in dimensional terms: the buoyancy flux, enters. The bulk statistics of the flow indicate a regime transition from WSBL to VSBL around $t^- > 6.8$ (cases S128–S256P): instead of a rather steady and smooth evolution for each case ($t^- \leq 6.8$), we now find sizeable oscillation in the bulk quantities. This is in agreement with previous findings in Ansorge and Mellado (2014): if strong stability is abruptly imposed on the flow, turbulence vanishes in vicinity of the wall (in the viscous sublayer, located next to the ground and around roughness elements), where mixing is attributed to viscous diffusion. The rapid change is followed by a somewhat slower recovery and an overshoot (at $t^- \approx 7.6$ for case S128P and $t^- \approx [9.2, 9.3]$ for cases S192P, S256P).

### 3.2 Wind Veer and Pressure-Driven Channeling

An over-veering of the surface wind, a rotation of more than 45°, is sometimes observed in particular under stably stratified conditions or for strongly anisotropic orography. With increasing stability, the turbulence intensity decreases along with buoyant destruction of turbulence and the velocity profile shifts to a more *laminar-like* profile with reduced velocity in the vicinity of the ground and an enhanced velocity in the upper part of the SBL. Hence, velocity gradients close to the ground and within the roughness are reduced and $u_\star(t)$ decreases (by approximately 15 %, cf. Figure 3a). Such reduced mixing comes with an increased surface wind veer $\alpha_\star(t)$ in Ekman flow which is known from both theoretical (Rossby and Montgomery 1935; Spalart 1989) and numerical (Coleman et al. 1992; Deusebio et al. 2014; Shah and Bou-Zeid 2014; Ansorge and Mellado 2014) consideration of the problem, see also KA24 (their Eq. 7). We evaluate the veering both throughout the domain ($\alpha(z,t)$) and at the surface ($\alpha_\star(t)$) as:

$$\alpha\left(z,t\right) \triangleleft \left(\left\langle \mathbf{u}\left(z\right)\right\rangle, \mathbf{g}\right), \tag{9a}$$

$$\text{and} \quad \alpha_\star\left(t\right) \triangleleft \left(-\boldsymbol{\tau}_\star\left(t\right), \mathbf{g}\right), \tag{9b}$$

where $\tau_\star(t)$ is the non-dimensional instantaneous, domain-averaged surface shear stress. Stability further increases the turning, measured in terms of $\alpha_\star$, that is already increased due to roughness in neutral conditions (cf. Sect. 4.4 in KA24): $\alpha_\star$ grows from $\approx 35°$ (case N) to 65° (S064, cf. Figure 3b). If we consider the SBL above $z^+ = H^+_{\max} + 5$, in other words above the roughness, the veering angle approaches approximately 40°, close to the laminar limit of 45°. A large portion of the increase in veering is concentrated within the roughness, where $\Delta\alpha$ (here, specified in the range of $0 \leq z^+ \leq H^+_{\max} + 5$) triples from $\approx 10°$ to $\approx 30°$.

For homogeneous, smooth surface conditions under stable stratification one would expect turning angles that are smaller than the laminar limit, viz. $\alpha_\star < 45°$. However, observations under certain orographic conditions indicate otherwise: In extended valleys (e.g. Upper Rhine

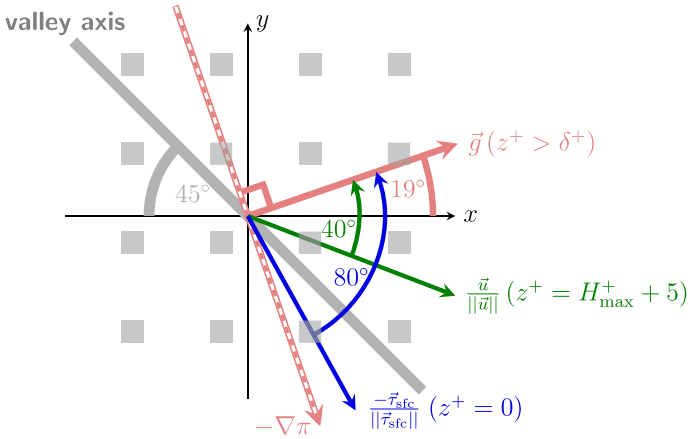


**Fig. 4** Schematic of the channeling mechanism for the case `S256P`, with the angles of the geostrophic wind ($z^+ > \delta^+$, red), the orthogonal pressure gradient (red dashed line), the horizontal velocity in the vicinity of the crests of the roughness elements ($z^+ = H^+_{\max} + 5$, green) and the angle of the surface shear stress on the lower wall of the domain ($z^+ = 0$, blue). Gray squares in the background depict the surface roughness

valley in Germany (Wippermann and Gross 1981), Tennessee valley in the USA (Whiteman and Doran 1993), region of the MISTRAL campaign (Weber and Kaufmann 1998)), the near-surface wind may turn by more than 90° with respect to the large-scale geostrophic wind (e.g. Wippermann and Gross 1981; Kalthoff and Vogel 1992. This phenomenon is termed *pressure-driven channeling* and was first described by Fiedler (1983), where the near-surface wind is observed to be preferably aligned with the valley axis in stable and low-wind conditions. Fiedler (1983) relates the cause of this mechanism to the valley-aligned component of the pressure gradient and friction on the side walls of the valley, while the Coriolis force was assumed to be negligible in this context. In our rough setup, three principal axes ('valleys') for the channeling mechanism exist: (i) the streamwise $x$-direction, (ii) the spanwise $y$-direction and (iii) the transverse direction, inclined by 45° to the roughness grid. The wind can flow through these 'valleys' more or less unimpeded by the surface roughness.

Our results indicate that option (iii) is relevant (cf. Figure 7c). The present results suggest an explanation of the channeling mechanism based on the momentum balance (cf. Figure 4): As stability increases, the wind speed within the roughness layer is substantially reduced (here, by approximately half, leading to a more *laminar-like* velocity profile, compare cases `N` vs. `S256P`) and, hence, the Coriolis and friction forces reduce. This results in a stronger turning of the wind in favour of the pressure gradient, which is the remaining large-scale forcing of the system. In our particular case, the large-scale forcing is shear-aligned for the smooth surface case, i.e. has an angle of $\alpha \approx 19°$ (KA24). Hence, the angle of the pressure gradient with respect to the 45°-axis is only $\approx 26°$, i.e. the projection of $\nabla\pi$ onto this 45°-axis is large. Therefore, we conclude that the triadic balance of the pressure gradient, friction and Coriolis forces determine the observed strong turning of the wind within the roughness, where the main mechanism for the super-rotation in the case of pressure-driven channeling is a reduction of the Coriolis force due to the reduced wind speed. We conclude that frictional effects alone do not explain the turning of the wind, and the balance of forces is only closed and consistent if the Coriolis force is considered—also within the roughness layer.

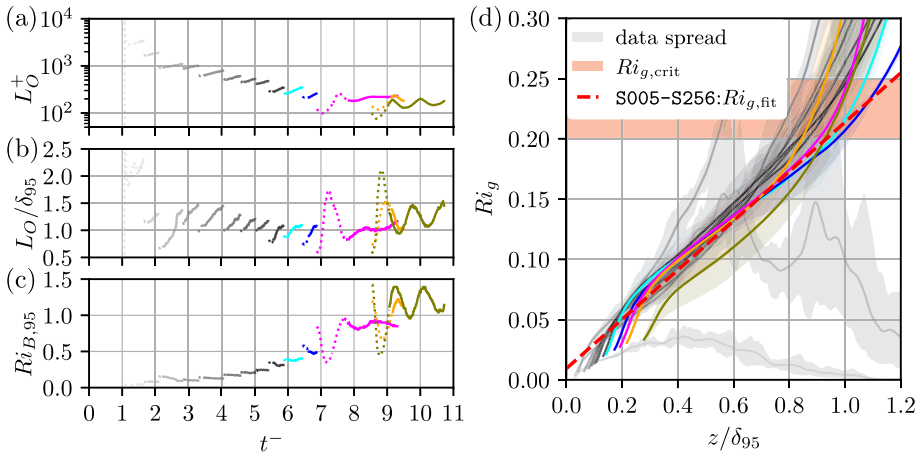


**Fig. 5** **a** Temporal evolution of the Obukhov length in viscous units $L_O^+(t^-)$ and **b** scaled in outer units with $L_O(t^-)/\delta_{95}(t^-)$. **c** Temporal evolution of the bulk Richardson number $Ri_{B,95} = B\delta_{95}/G^2 = Ri_\Lambda \delta_{95}/\Lambda_{Ro}$. Dotted lines are excluded from the analysis, since these parts are identified as initial transients. **d** Time-averaged gradient Richardson number $Ri_g = (\partial_z\langle\overline{b}\rangle)/\left[(\partial_z\langle\overline{u}\rangle)^2 + (\partial_z\langle\overline{v}\rangle)^2\right]$, plotted as a function of the mean non-dimensional height $z/\delta_{95} > H_{\max}/\delta_{95}$ of the stable cases. The red dashed line indicates the linear fit for the cases `S005-S256P` for $0.35 < z/\delta_{95} < 0.7$ with $Ri_{g,\mathrm{fit}} = 0.01 + 0.2z/\delta_{95}$, the red shaded area depicts the range of the critical Richardson number $Ri_{g,\mathrm{crit}} = 0.2 - 0.25$ according to the literature, and the shaded regions corresponds to the spread of the data

### 3.3 Obukhov Length

At a height $z = L_O$ (cf. 7a), the buoyant destruction of TKE equals its mechanical shear generation, under the prerequisite that fluxes are truly constant; for the boundary layers studied here, this is an approximation that is commonly used when interpreting data in the context of ASL similarity. Hence, absent pressure redistribution and transport effects, the shear generation dominates for $z \lesssim L_O$. Alternatively, $L_O$ is the largest wall-attached eddy for which the kinetic energy is sufficient to overcome stratification (Van de Wiel et al. 2008).

Flores and Riley (2011) propose the buoyancy Reynolds number $Re_L \equiv L_O^+$ as scaling parameter to indicate turbulence collapse in a hydraulically smooth SBL. They find that the flow laminarizes for $Re_L < Re_{L,\mathrm{crit}} \approx 40$ which implies $L^+_{O,\mathrm{crit}} = Re_{L,\mathrm{crit}}/\kappa \approx 100$. In the case of rough walls, they suggest $L_{O,\mathrm{crit}}/h_r \approx 1$ as an appropriate criterion, where $h_r$ is a characteristic roughness length scale. Here, the roughness length $h_r \mathrel{\widehat{=}} H$ is the mean height of the roughness elements, in viscous units $H^+ \approx 30 - 40$ (with the range of $u_\star(t)$ in Fig. 3a). By coincidence, both suggested criteria are equivalent given our setup. In the current study, we do not observe a complete laminarization of the flow since the most stable cases at $t^- \approx 8.7$ drop to $L_O^+ \approx 75$ (Fig. 5a). These cases are close to laminarization and hence, it is a strong indicator of the intermittent regime, where turbulent and laminar regions coexists in the flow. As previously discussed, the flow is effected by buoyancy for $t^- > 2.1$, where the ratio $L_O/\delta_{95} < 1$ for the first time (Fig. 5b). Here, buoyancy is the dominating process, since $L_O \lesssim \delta_{95}$. Interestingly, for the very stable case `S128P` at $t^- > 8$ the ratio $L_O/\delta_{95} \approx 1$, whereas cases `S192P`, `S256P` oscillate with a damped amplitude (observable for case `256P`) around the value $L_O/\delta_{95} \approx 1.1{-}1.2$.

### 3.4 Richardson Number

An important indicator for the collapse of turbulence in stably stratified flow is the local gradient Richardson number, defined as:

$$Ri_g = \frac{\partial\langle b\rangle/\partial z}{(\partial\langle u\rangle/\partial z)^2 + (\partial\langle v\rangle/\partial z)^2}, \tag{10}$$

with a 'critical' range of $Ri_{g,\mathrm{crit}} \approx 0.2 - 0.25$ (Garratt 1992), where the precise value and nature of the threshold is still a matter of debate (cf. extensive discussion in Sect. 4.2, Grachev et al. 2013). The flow regime we find for the stable cases S005–S256P (Fig. 5d) is in accordance with previous findings regarding their Richardson number. The cases pass the range of 0.2–0.25 for $0.8 < z/\delta_{95} < 1.1$. Above the boundary layer thickness $\delta_{95}$, the flow is mostly laminar. Within the boundary layer $Ri_g$ approximately follows a linear relation (cf. red dashed line in Fig. 5d). The cases S001–S002 do not reach $Ri_{g,\mathrm{crit}}$ and are therefore slightly effected by buoyancy. With respect to both field observation and numerical bulk models of the SBL, the bulk Richardson number is a key parameter. We use here $Ri_{B,95}$ based on $\delta_{95}$ (Fig. 5c). While $Ri_B \ll 1$ for near-neutral cases where buoyancy acts as a passive scalar, it reaches 1 for the most stable cases indicating that (i) our study spans the full range of stability regimes *and* (ii) the criticality of stability is well reproduced in our rough setup, also in terms of the bulk Richardson number.

### 3.5 Synopsis of the Turbulent Flow

Visual inspection of instantaneous snapshots of enstrophy $\xi(x_i)$ for the neutral case N at $t^- \approx 1.1$, weakly stable case S008 at $t^- \approx 3.5$ and very stable case S256P at $t^- \approx 8.8$ (Figs. 6, 7) reveal the antagonistic interplay of static stability and small-scale surface roughness despite the small blocking ratio ($H/\delta_N \approx 0.015$ for case N).

Immediately above the roughness elements, strong vortical activity is observable (Fig. 6a, b), indicative of the buffer-layer (for homogeneous surfaces at $5 < z^+ < 30$, according to Pope (2000); here, elevated by the roughness height). Here, turbulent production peaks and the fine turbulent structures move upwards while increasing in size until the boundary layer height is reached (blue bars in Fig. 6 for $\delta$ and $\delta_{95}$). Non-turbulent fluid from aloft is entrained deeply into the boundary layer (cf. light regions in Fig. 6a, e.g. at $1 \lesssim t^- \lesssim 1.5$). Simultaneously, ejections of turbulent fluid penetrate into the upper part of the boundary layer. This phenomenon is inherent to boundary layer flow and related to the external intermittency of the turbulent Ekman flow (Ansorge and Mellado 2014).

The suppression of turbulence by buoyancy reduces the boundary layer height of case S008 (Fig. 6b), measured in terms of $\delta_{95}$, by half in comparison to N, whereas $\delta$ is reduced by approximately 10 %. It is distinctly recognizable that $\delta_{95}$ rather than $\delta$ is the appropriate scale of the boundary layer thickness in the presence of stable density stratification. Large-scale structures are still visible for S008 at $z > \delta_{95}$ above the boundary layer, which is attributed to residual turbulence inherited from case N. A further increase in stability leads to a strong reduction in turbulence activity in the VSBL for case S256P (Fig. 6c) with a boundary layer thickness of $\delta_{95} \approx 3H$. In this case the boundary layer becomes very thin and there is a complex interplay between gravity waves, residual turbulence and large-scale intermittency which is probably not relevant at atmospheric scale due to the mismatch in scale separation vide the reduced Reynolds number of our setup.

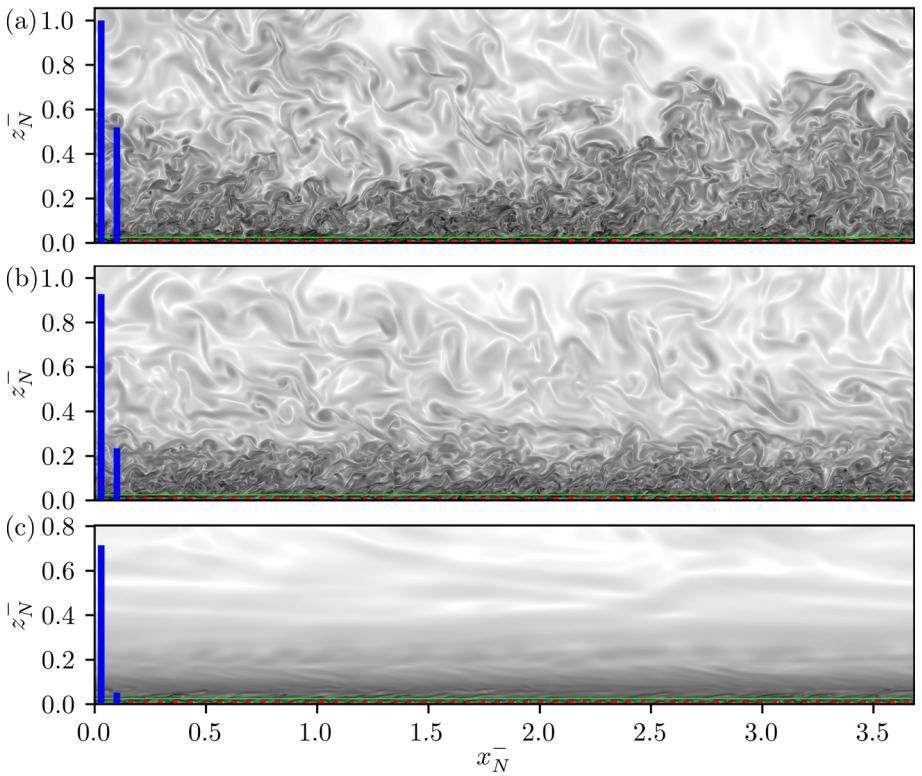


**Fig. 6** Streamwise-vertical, instantaneous intersection of the logarithm of the enstrophy $\xi(x_i)$ with a linear colormap $0 \leq \xi \leq 16$ of **a** case `N`, **b** case `S008`, and **c** case `S256P`; time corresponds to circles in Fig. 3. The axes are scaled with the neutral boundary layer thickness and blue bars depict the instantaneous boundary layer thickness $\delta_\star(t)$ and $\delta_{\star,95}(t)$. The roughness elements on the ground are shown as red cuboid blocks. Green lines for the vertical position of Fig. 7d–f

Within the surface roughness (at half the height of the elements) and above the roughness, located at the lower bound of the surface e.g. logarithmic layer, no distinct differences are visible between the cases `N` and `S008` (Fig. 7a, b, d, e). The flow is turbulent inside the roughness, due to the high Reynolds number of the flow and instabilities induced by the roughness elements (Fig. 7a,b). Above (Fig. 7d,e), the turbulence is homogeneous with the imprint of hairpin vortices seen as elongated enstrophy filaments. Hairpins originate from the buffer layer and are characteristic for wall-bounded flows in the logarithmic layer (Adrian 2007). In conclusion, the visual appearance of the turbulence in the close-wall region is comparable for the neutral and weakly stable regime, which is consistent with the literature (García-Villalba and del Álamo 2011; Watanabe et al. 2019; Atoufi et al. 2021), despite the reduction in $\delta_{95}$ and the stronger turning angle $\alpha$. In case of very strong stability, heavy fluid is trapped inside the roughness and therefore, the surface layer is decoupled from the outer layer (Van de Wiel et al. 2012a). Weak turbulence activity is visible within the roughness, which is induced by the transverse flow ($\approx 45°$) of the objects with sharp edges (Fig. 7c). Above the roughness, the intermittent behaviour of the flow is clearly observable (Fig. 7f), where patches of turbulent fluid (regions with sharp transitions) are embedded in non-turbulent fluid (smeared regions). Global intermittency in the VSBL appears in space and time, and

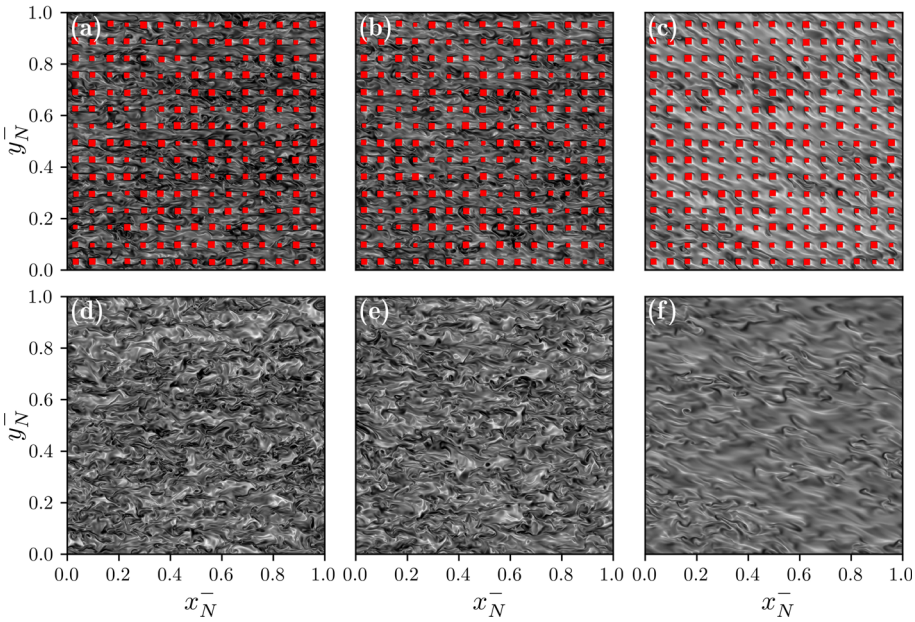


**Fig. 7** Horizontal (streamwise-spanwise) intersection of the size $[\delta_N \times \delta_N]$, corresponding to approximately 1/14 of the computational domain (time instances cf. circles in Fig. 3) with a linear colormap $5 \leq \xi \leq 15$ (cf. explanations in Fig. 6, identical turbulent fields are chosen). Shown are the cases **a**, **d** `N`, **b**, **c** `S008` and **c**, **f** `S256P` at half height of the roughness elements (**a**–**c**) $z_N^+ \approx 20$ and in the surface layer at $z_N^+ \approx 65$ [(**d**–**f**), cf. green lines in Fig. 6]

is not an on–off process (Mahrt 2014; Ansorge and Mellado 2014). In order to investigate this behaviour, computational domains of sufficient size are required that can accommodate these laminar-turbulent patterns (Deusebio et al. 2014), which is the case here.

### 3.6 Maximum Sustainable Heat Flux

The heat (buoyancy) flux $\langle w'b' \rangle$ represents at the same time also the buoyant destruction (production) term in the TKE budget equation, and it is limited from two-sides given a large-scale forcing (De Bruin 1994). In the WSBL, the vertical mean temperature profile is nearly neutral with a small gradient, and turbulent mixing is strong. In these conditions, heat flux is limited due to lack of temperature contrast, i.e. $\langle b'b' \rangle$. The other extreme is the VSBL, where the restoration of buoyant forces is so strong that turbulent mixing in the boundary layer is inhibited and the heat flux is limited for lack of velocity fluctuations $\langle w'w' \rangle$. In between these two extrema, the heat flux assumes a maximum according to the concept of the *maximum sustainable heat flux* (MSHF) Van de Wiel et al. (2012a, b).

The core of the MSHF concept is confirmed by the current simulations (Fig. 8). However, we observe for the vertically integrated buoyancy term of the TKE budget a pronounced plateau over two orders of magnitude in $Ri_\Lambda$ rather than a distinct maximum, which differs from stable Ekman flow over smooth surfaces, where the plateau width is less than one order of magnitude in $Ri_\Lambda$ (cf. Fig. 6c, Ansorge and Mellado 2014).

This characteristic behaviour of $\langle w'b' \rangle$ as a function of the stability, underpins the importance of roughness as a very efficient triggering mechanism of turbulence due to flow

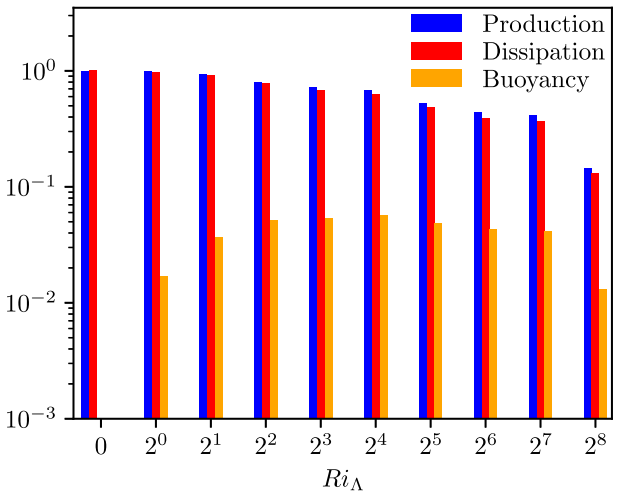


**Fig. 8** Domain-wise, vertically integrated contributions to the TKE budget (shear production, buoyancy destruction and dissipation of TKE). Bounds for vertical integration are $H_{\max}$ to $L_z$ as a function of the external Richardson number $Ri_\Lambda$. Terms are normalized with the neutral production rate. The integration is shown for $\Delta t^- \approx 0.1$ around the time instances depicted as $\times$-symbols in Fig. 3 (not all cases are considered)

instabilities on sharp edges (detached eddies), which counteracts efficiently buoyancy induced reduction of turbulence and is assumed to form the observed plateau. The remaining imbalance of the presented TKE terms (shear production, dissipation, buoyancy destruction) in Fig. 8, especially for the more stable cases, are the integrated temporal tendency and transport terms of the TKE budget (not shown). These terms are non-zero, as the more stable cases are out of equilibrium to a certain degree.

## 4 Surface-Layer Similarity

For guidance in the subsequent gradient analysis, Fig. 9 present horizontal velocity and buoyancy profiles with increasing stratification. In contrast to non-rotating flow problems, the horizontal mean velocity profiles in Ekman layers exhibit a super-geostrophic velocity, referred to as the low-level jet (LLJ) (Fig. 9a). With increasing stability, the height of the LLJ maximum is reduced from $z_N^- \approx 0.4$ for the neutral case `N` to $z_N^- \approx 0.1$ for the most stable case `S256P`, with a velocity increase of $\approx 4\,\%$ (`N`) up to $\approx 20\,\%$ (`S064`) with respect to the geostrophic velocity. The reduction in the vertical LLJ position is accompanied by a reduced boundary layer thickness (cf. Figures 3a, 6), which also reduces the outer length scale relevant for the formation of turbulence. Due to the increased shear and turbulence triggering by roughness, also the inner length scale of the turbulent boundary layer is reduced, such that a turbulent boundary layer is maintained. While our data suggest the thickness of the surface layer is marginal for the most stable cases, this cannot be judged based on surface scales alone. Hence, the following discussion assumes existence of a surface layer, which is common when using surface layer similarity in an observational, operational, or modelling context. Within the roughness (indistinguishable in Fig. 9a) at $z_N^- \lesssim H$, the velocity reduces with increasing stability, whereas for $z_N^- \gtrsim 2H$ the velocity enhances with increasing stability. Here, above the roughness ($z_N^- \gtrsim 2H$), the velocity gradient increases due

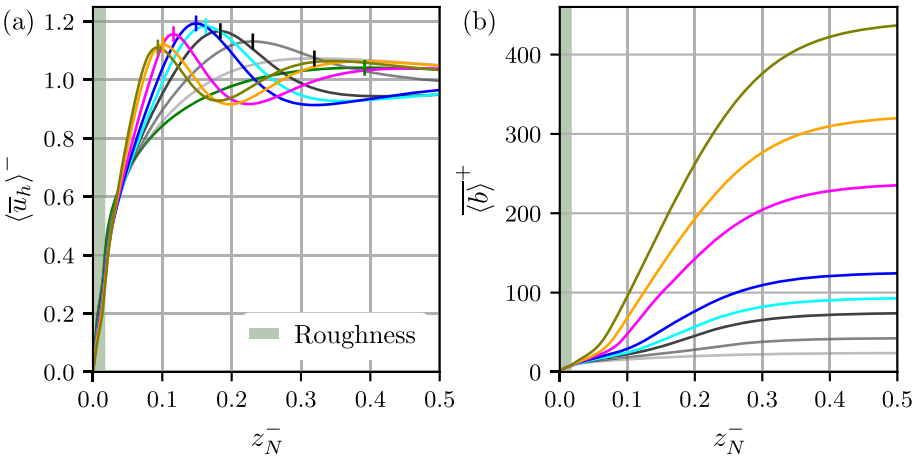


**Fig. 9** **a** Horizontal mean velocity and **b** buoyancy profiles (normalized with $b_\star(t)$) of the stable cases `S004`, `S012`, `S032-S256P`, case `N` only in (**a**) (green). The vertical strokes in (**a**) depict the position of the super-geostrophic velocity. Temporal averaging according to the intervals in Fig. 3. The vertical distance is normalized with the turbulent boundary layer thickness of the neutral case (`N`) as reference. The green shaded areas depict the maximum height of the surface roughness

to less vertical mixing. With increasing stratification ($Ri_\Lambda$) the buoyancy profiles steepen, respectively the gradient increases. Above the boundary layer thickness, where diffusion dominates (approximately the position of the LLJ) buoyancy increases linearly and then flattens (Deusebio et al. 2014).

### 4.1 ASL Similarity in Vicinity to the Rough Boundary

MOST, the corner stone of ASL similarity (Obukhov 1971; Foken 2006), is limited to horizontally homogeneous and statistically stationary conditions (ASL, Obukhov 1971; Ansorge 2019). It further precludes that the stability (e.g. measured in terms of $Ri$) does not exceed a critical value $Ri_{\text{crit}}$ and neglects the vertical flux divergence due to the Coriolis force, leading to the so-called *constant flux layer* (maximum of the total turbulent flux varies less than 10%, cf. Stull 1988) or *channel-flow analogy*. In KA24 we show that the neglect of the Coriolis force in the ASL is a strong assumption for intermediate $Re$, where the share of the Coriolis term in the total drag is up to 10 % at the top of the roughness elements. Obviously, this assumption becomes even stronger in stratified conditions where the ABL height decreases in response to surface cooling. We intend here to also reach the regime of extreme stability where not only the scale separation shrinks and existence of a surface layer becomes questionable in general, but also the stability correction exceeds the order of one, which is a fundamental problem from the perspective of flux parameterization. Nonetheless, in the following, we stick to the common height range defined in terms of the friction thickness $\delta_\star$, which requires caution when interpreting data for strongly stable cases at the larger end of the stability parameter ($\zeta$, defined below). In fact, ASL closures implied by MOST are ubiquitous in numerical models at all scales, and even if requirements are not fully met (e.g. for complex terrain, the non-stationarity of the ABL, etc.), observations confirm to the theory (Grachev et al. 2013; Stiperski and Calaf 2018).

Within the ASL, MOST implies that appropriately non-dimensionalized gradients of the horizontal wind speed, $u_\mathrm{h}(z) = \sqrt{\langle u\rangle^2 + \langle v\rangle^2}$, and buoyancy, $b(z)$, depend on a non-dimensional height only, namely:

$$\zeta_i = \kappa_i (z - d_i)/L_O, \tag{11a}$$

(here the von Kármán constants are included, since $L_O$ is formulated without). Based on the TKE equation, $\zeta$ can be interpreted as a stability parameter representative of an eddy size beyond which stability effects exceed inertia. The index $i$ corresponds to $(\cdot)_\mathrm{m}$ for momentum or $(\cdot)_\mathrm{h}$ for heat, reflecting the different von Kármán constants ($\kappa_\mathrm{m} = 0.42$, $\kappa_\mathrm{h} = 0.35$). KA24 found different displacement heights for momentum and heat, but an overall small dependence of the $L_2$ error on the particular value. Here, we therefore stick to the common assumption $d_\mathrm{h} = d_\mathrm{m} \equiv d$ and use $d/H = 2/3$. For the non-dimensionalized gradients $\Phi_\mathrm{m}(\zeta_\mathrm{m})$ and $\Phi_\mathrm{h}(\zeta_\mathrm{h})$ we obtain:

$$\frac{\kappa_\mathrm{m}\,(z-d)}{u_\star}\sqrt{\left(\frac{\partial\langle u\rangle}{\partial z}\right)^2 + \left(\frac{\partial\langle v\rangle}{\partial z}\right)^2} = \Phi_\mathrm{m}\,(\zeta_\mathrm{m})\,, \tag{11b}$$

$$\frac{\kappa_\mathrm{h}\,(z-d)}{b_\star}\frac{\partial\langle b\rangle}{\partial z} = \Phi_\mathrm{h}\,(\zeta_\mathrm{h})\,. \tag{11c}$$

The existence of such unique representations $\Phi_i(\zeta_i)$ is understood to indicate the suitability of the assumptions of the constant-flux layer. The dependencies of $\Phi_\mathrm{m}$ and $\Phi_\mathrm{h}$ on $\zeta_\mathrm{m}$ and $\zeta_\mathrm{h}$, respectively, describe the stability dependence of the velocity and scalar profiles. In neutrally stratified flow with $\zeta_i = 0$ (since $L_O \to \infty$), the logarithmic law of the velocity emerges with $\Phi_\mathrm{m}\,(\zeta_\mathrm{m} = 0) = 1$, whereas $\zeta_i > 0$ for stably stratified flow. Based on observational studies, the Businger–Dyer relations (Businger et al. 1971; Dyer 1974; Garratt 1992):

$$\Phi_\mathrm{m}\,(\zeta_\mathrm{m}) = \alpha_\mathrm{m} + \beta_\mathrm{m}\zeta_\mathrm{m}, \tag{12a}$$

$$\Phi_\mathrm{h}\,(\zeta_\mathrm{h}) = \alpha_\mathrm{h} + \beta_\mathrm{h}\zeta_\mathrm{h}, \tag{12b}$$

are widely accepted for the weakly stable regime ($\zeta_i \ll 1$). The empirical parameters are $\alpha_\mathrm{m} = 1$, $\alpha_\mathrm{h} = 0.74$ and $\beta_\mathrm{m} = \beta_\mathrm{h} = 4.7$ (Högström 1988, 1996; commonly approximated with $\beta_i \approx 5$).

We find reasonable agreement with these observational fits for stability corrections $\zeta \lesssim 1$ (Fig. 11). As mentioned above, results for stronger stability should be interpreted with caution, which is in fact seen by an increased spread for higher stability and a systematic deviation from the ASL fits in Fig. 10.

This also agrees with previous DNS of Ekman flow over smooth surfaces (Ansorge and Mellado 2014; Shah and Bou-Zeid 2014; Ansorge 2019) and LES of Ekman flow with subsidence (Bon et al. 2024). The best fits for the non-dimensional gradients of wind speed and buoyancy are:

$$\Phi_\mathrm{m}(\zeta_\mathrm{m}) - \alpha_\mathrm{m} = 5.3\zeta_\mathrm{m}, \tag{13a}$$

$$\Phi_\mathrm{h}(\zeta_\mathrm{h}) - \alpha_\mathrm{h} = 12.5\zeta_\mathrm{h}, \tag{13b}$$

respectively, where we estimate $\alpha_\mathrm{m} = 0.89$ and $\alpha_\mathrm{h} = 0.72$ (cf. discussion in the Appendix 1). The analysis here is exempt from the exact value of the parameters $\alpha_i$. In terms of $\zeta_\mathrm{m}$, we find $\Phi_\mathrm{h}(\zeta_\mathrm{m}) - \alpha_\mathrm{h} = 10.5\zeta_\mathrm{m}$ for cases `S001-S064`. In many practical applications of ASL theory, $\zeta_\mathrm{h}$ is approximated by $\zeta_\mathrm{m}$ due to the lack of informative models for turbulent

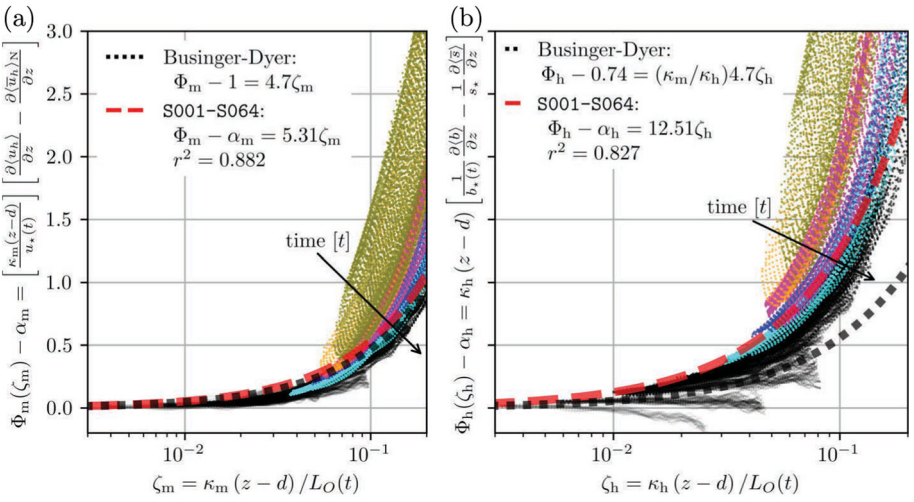


**Fig. 10** Non-dimensional gradients of the **a** horizontal velocity and **b** buoyancy, as a function of the stability parameter $\zeta_m$, $\zeta_h$, according to (11). The data in the regime $z^+_{\log,i} \leq z^+ \leq 0.1Re_\tau$ is instantaneous and spatially averaged in the horizontal, while using the respective instantaneous friction values of $u_\star(t)$, $b_\star(t)$ (respectively $s_\star$ for the neutral case N) and the Obukhov length $L_O(t)$. The linear regression functions (red dashed lines, with the $r^2$-value, the coefficient of determination) are derived in consideration of the cases S001-S064 with a zero-plane displacement of $d/H = 2/3$. The arrows (*time*) depict the temporal evolution

diffusivity. We use $d_h = d_m$, which implies:

$$\Phi_h(\zeta_m) = \alpha_h + \frac{\kappa_h}{\kappa_m}\beta_h\zeta_m. \tag{14}$$

The data is fitted in the regime $z^+_{\log,i} \leq z^+ \leq 0.1Re_\tau$, with the lower boundary of the logarithmic layer at $z^+_{\log,i} = 30 + d_i^+$ (KA24) and the commonly accepted limit of the upper boundary of the ASL with approximately 10 % of $\delta_\star$.

Cases with stronger stability fall into the very stable regime where a linearization of the stability correction $\Phi_m - \alpha_m$ (magenta, orange, olive coloured cases) is no longer appropriate (Mahrt 2014) for the limited extent of the ASL and large effects of stability. While outside the ASL in terms of strict criteria ($\delta_{95}$, cf. Fig. 6), the very stable data of the cases S128P-S256P show a distinct left curvature (cf. Ansorge 2019, Fig. 12). As the simulation time progresses, a tendency is observed to the right, closer to the linear fit, indicating that the left curvature for large values of the stability parameter ($\zeta > 0.1$) is a transient effect reflecting the imbalance of the ABL with the surface boundary condition.

The linear fit of $\Phi_m$ is very close to the widely-used Businger–Dyer relation, whereas $\Phi_h$ does not agree. We attribute this disagreement to insufficient convergence, respectively, the nonequilibrium state of the data for large stratification, since the linear fit improves if only the weakly stable cases S001-S005 are considered ($\beta_h = 4.9$). We further note that also Högström (1988) estimates $\beta_h \approx 8$ after eliminating systematic errors from observational data.

For large stratification, the linear stability correction is known to deviate in the very stable regime, due to its highly non-stationarity (inertial oscillation, adaptation of the turbulent boundary layer to strongly modified surface boundary, intermittency) and strong turning of the wind within the substantially decreasing boundary layer thickness (Fig. 3). Moreover,

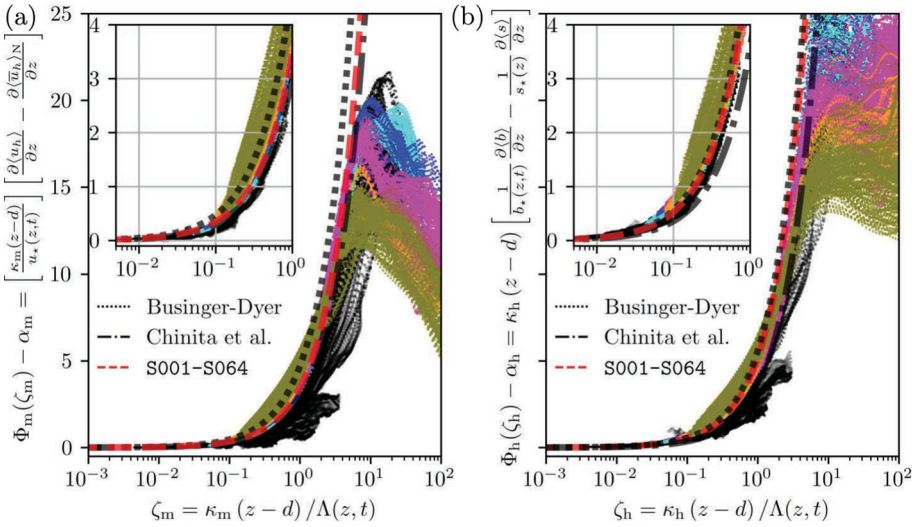


**Fig. 11** Similar to Fig. 10. Here, with the instantaneous and local (in the vertical) values of $u_\star(z,t)$, $b_\star(z,t)$, $\Lambda(z,t)$, according to the local theory of Nieuwstadt (1984). The close-up views and the similarity functions are fitted up to the height $z^+ < 0.1\delta_\star$, and data is plotted up to $z^+ < 0.3\delta_\star$. **a** Lines: Businger–Dyer relation, $\Phi_\mathrm{m} - 1 = 4.7\zeta_\mathrm{m}$ (black dotted line); Chinita et al. (2022) $\Phi_\mathrm{m} - 1 = 3\zeta_\mathrm{m}$ (black dotdashed line); S001-S064, $\Phi_\mathrm{m} - \alpha_\mathrm{m} = 3.45\zeta_\mathrm{m}$ (red dashed line) with $r^2 = 0.97$. **b** Lines: Businger–Dyer relation, $\Phi_\mathrm{h} - 0.74 = 4.7\kappa_\mathrm{m}\kappa_\mathrm{h}^{-1}\zeta_\mathrm{h}$ (black dotted line); Chinita et al. (2022), $\Phi_\mathrm{h} - 0.74 = 3\kappa_\mathrm{m}\kappa_\mathrm{h}^{-1}\zeta_\mathrm{h}$ (black dotdashed line); S001-S064 $\Phi_\mathrm{h} - \alpha_\mathrm{h} = 5.21\zeta_\mathrm{h}$ (red dashed line) with $r^2 = 0.981$

turbulence is observed to be highly anisotropic, respectively of non-Kolmogorov type (Stiperski and Calaf 2018). Then, the surface flux seizes to be a relevant scaling parameter, and we follow the local scaling approach of Nieuwstadt (1984) (cf. Fig. 11), while using local values of the Obukhov length $\Lambda(z,t)$ for the stability parameters $\zeta_i$ and the local friction values $u_\star(z,t)$, $b_\star(z,t)$ for the stability functions $\Phi_i$. This approach yields a better collapse of the data compared to Fig. 10, since the scattering of data is significantly reduced. Chinita et al. (2022) proposes for the local MOST based on LES simulations the parameters $\beta_i \approx 3$ (rather than $\beta_i \approx 5$). Notably, the very stable cases do follow the proposed linear stability correction functions as well, even though, according to strict criteria, some values originate from above the ASL. Anyhow, the values of $\beta_\mathrm{h}$ in the weakly stable and moderately stable regimes are higher compared to the proposed value. Again, this is assumed to be related to limited simulation times and insufficient convergence.

In the context of the local scaling approach, the very stable cases indicate a right curvature of the data with respect to the linear fits, which is in accordance to observations (e.g. Chenge and Brutsaert 2005; Grachev et al. 2013, ). For $\zeta_i \gg 1$ a *levelling-off* of $\Phi_i$ (Fig. 11) is observed, while $\Phi_\mathrm{m}$ reaches a peak and continues with a negative slope and $\Phi_\mathrm{h}$ forms a plateau. Peak and plateau values of $\Phi_i$ decrease with increasing stability of the cases. Mahrt (2007) links this characteristic with a simultaneous increasing stability and non-stationarity of the flow (wave-like, meandering motions) and thus an enhanced mixing efficiency. As a result, the slope $\Phi_i$ decrease for large $\zeta_i$, whereas this behaviour is pronounced for momentum compared to buoyancy. However, the data are presented up to the upper bound $0.3\delta_\star$, which is outside the very stable boundary layer, measured in terms of $\delta_{\star,95}$ (cf. Figure 6), and is thus associated with problems in LES and observations where the first model layer or the first

measurement point under strongly stable conditions could as well lie outside the boundary layer.

Surface roughness increases $u_\star$ in comparison to a smooth surface with similar forcing of the flow. Hence, the scale separation measured in $Re_\tau$ is enhanced, which results in a deeper logarithmic layer. As a consequence of the rise of $Re_\tau$, we observe a higher degree of consistency of our data for a wider range of stability in contrast to the smooth case at similar $Re_D$ (cf. Ansorge 2019, Fig. 12). The induced growth in scale separation by roughness is counteracted by increasing stability, since it reduces the extent of the remaining logarithmic layer until a critical value, here $Ri_\Lambda > 64$, is reached from where measurements deviate from the theory.

### 4.2 Non-dimensional Gradients in the Roughness Region

The validity of MOST is limited to the inertial sublayer. Hence, classic surface-layer similarity only holds above the top of the roughness elements. This is in part for theoretical reasons, but also due to practical limitations, as in the field, it is virtually impossible to obtain data within small-scale roughness. Here, we briefly report on the scalings observed below the height of the roughness elements. In the lower part of the roughness region, i.e. below $z^+ \approx 10$, the velocity gradients appear to fall in a narrow band that grows linearly with distance from the wall (Fig. 12a). This suggests that the viscous law of the wall is appropriate here. The classical scaling $u^+ = z^+$ would be re-covered if a truly wall-based velocity scale would be considered, i.e. if the friction velocity were calculated from the bottom shear alone. Near the top of roughness elements, the scaling is not universal and would need to include information on the velocity scale at the top of the roughness elements. Interestingly, the transition of the velocity profile to the different velocities in the outer region (higher for stronger stability) is mostly confined to the upper region of the roughness region, where a strong stability-dependence is observed. This dual behaviour suggests that it will not be possible to prescribe profiles in the roughness region by either a wall-based or a surface-layer-base scaling; instead, a complete description will need to resort to a mixed scaling incorporating information from the friction at the top of the roughness elements and the friction at the actual domain bottom. The partitioning of friction between the top of roughness elements and the actual domain bottom is hence a key parameter to determine the dynamics within the roughness region.

The scalar profiles show a similar duality suggesting wall-based scaling below $z^+ \approx 10$ and profile-dependency above. Interestingly, there is a maximum in the scalar gradient around $z^+ \approx 10$ and a plateau and collapse of data (cases `S001-S064`) for the non-dimensional buoyancy gradients (Fig. 12b). The plateau is located above the viscous sublayer $z^+ > 5$ and below the lowest roughness elements, here limited to $z^+ < 20$ with a value of 0.76, which is close to $\alpha_\mathrm{h}$. This maximum of the gradient is related to a local minimum of turbulent scalar transport, and we suppose it is due the separation of the mixing at the roughness tops from the mixing at the domain bottom. Apparently, this separation is stronger for buoyancy (which shows a local maximum) than it is for momentum (which only shows a right curvature in the profile at the respective height). This difference underlines the critical role of pressure (blocking) effects in the roughness region which are the root cause for differences between scalar and momentum quantities and cause a stability and height-dependence of the turbulent Prandtl number (cf. Sect. 4.4).

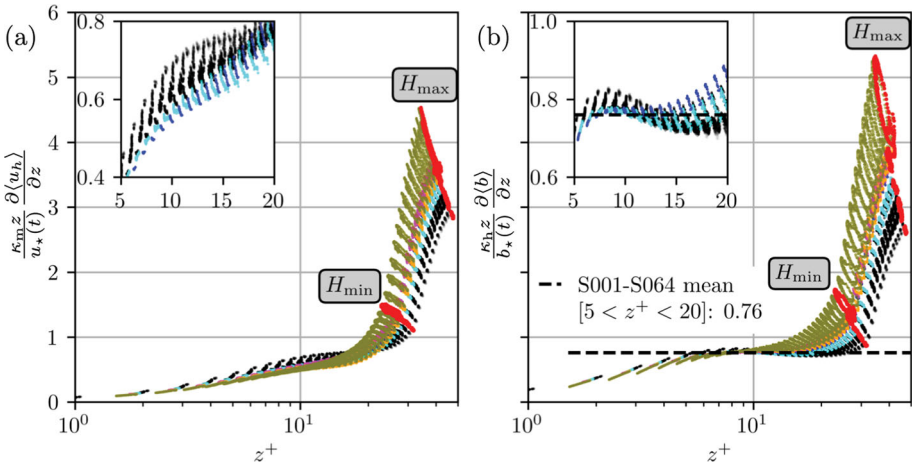


**Fig. 12** Non-dimensional gradients of the **a** horizontal velocity and the **b** buoyancy within the reach of the roughness elements ($H_{\min}$ and $H_{\max}$ depict the distribution of roughness element heights, red markers), plotted against the vertical distance in viscous units $z^+$. The presented data is instantaneous and horizontally averaged, while using the respective instantaneous values of $u_\star(t)$, $b_\star(t)$. **b** The mean value is derived in consideration of the cases `S001-S064` in the range $5 < z^+ < 20$

### 4.3 Reynolds Number Effects on the ASL Similarity

ASL theory commonly neglects viscous effects for the very high Reynolds number encountered in geophysical problems. For typical scales of the neutral ABL, the magnitude of $Re_{\mathrm{ABL}}$, indicative of the scale separation in a neutrally stratified atmosphere, is $\mathcal{O}(10^8)$ (Mellado et al. 2018). With increasing stability and thus decreasing depth of the ABL (cf. Figure 3a), the relevant scale separation $Re_{\mathrm{ABL}}$ is reduced and viscous effects may matter, at least to some extent. For the intermediate Reynolds number of our setup ($Re_\tau \approx$1800–2700), we expect viscous stress to be non-negligible in the ASL theory at strong stability. While this is not necessarily the case in atmospheric conditions, we need to consider those viscous effects to allow for an uncontaminated formulation of the similarity theory with respect to the actual geophysical scale separation. We, however, note that close to the surface these effects also occur in the atmosphere which may be relevant for some very high-resolution LES studies with resolutions on the sub-metre scale. Further, this section makes use of the common assumption that it is the total stress, total vertical gradient and total horizontal velocity which scale in the context of surface-layer similarity. While this is certainly an increasingly strong assumption for stratified flow, it is consistent with the way in which surface-layer similarity is commonly applied.

The total stress $\tau_{\mathrm{tot}}$ in the boundary layer is composed of the viscous and turbulent stress, which in our non-dimensionalized formulation reads as:

$$\tau_{\star,\mathrm{tot}} = \tau_{\star,\mathrm{visc}} + \tau_{\star,\mathrm{turb}} = \frac{1}{Re_\Lambda} \frac{\partial \langle u_\mathrm{h} \rangle}{\partial z} + \sqrt{\langle u'w' \rangle^2 + \langle v'w' \rangle^2}. \tag{15a}$$

Here, we consider the horizontal velocity and total vertical flux, since the veering of the wind within the surface layer is substantial. Commonly, the turbulent stress is modelled with the eddy viscosity approach introduced by Boussinesq (cf. Sect. 3.4.1 on p.171, Rotta 1972),

where the turbulent flux is related to the local vertical mean gradient, given by:

$$\tau_{\star,\mathrm{turb}} = -K_{\star,\mathrm{m}} \frac{\partial \langle u_\mathrm{h} \rangle}{\partial z}, \tag{15b}$$

$$\text{with: } K_{\star,\mathrm{m}} = l_{\star,\mathrm{m}}^2 \frac{\partial \langle u_\mathrm{h} \rangle}{\partial z}. \tag{15c}$$

The eddy viscosity $K_{\star,\mathrm{m}}$ is modelled with the mixing length $l_{\star,\mathrm{m}}$, where the simple relation $l_{\star,\mathrm{m}} = \kappa_\mathrm{m} z$ (Prandtl 1925) is used. Therefore, $K_{\star,m}$ is the eddy viscosity non-dimensionalized by $G\Lambda_{Ro}$, and not constant but rather a function of time and space. The non-dimensionalized total shear stress $\tau_{\star,\mathrm{tot}}$ (15a) is given by:

$$\tau_{\star,\mathrm{tot}} = \frac{\partial \langle u_\mathrm{h} \rangle^+}{\partial z^+} + \left(\kappa z^+\right)^2 \left(\frac{\partial \langle u_\mathrm{h} \rangle^+}{\partial z^+}\right)^2 = \frac{\partial \langle u_\mathrm{h} \rangle^+}{\partial z^+} + \left[\Phi_{\mathrm{m,cor}}\left(\zeta_\mathrm{m}\right)\right]^2, \tag{15d}$$

whereas $\Phi_{\mathrm{m,cor}}$ is the stability function (11b) corrected by the viscous stress and hence,

$$\Phi_{\mathrm{m,cor}}\left(\zeta_\mathrm{m}\right) = \Phi_\mathrm{m}\left(\zeta_\mathrm{m}\right) - \sqrt{\frac{\partial \langle u_\mathrm{h} \rangle^+}{\partial z^+}} = \alpha_\mathrm{m} + \beta_{\mathrm{m,cor}} \zeta_\mathrm{m}. \tag{16a}$$

In this reading, $\Phi_{\mathrm{m,cor}}$ corresponds to the actual non-dimensional gradient in the context of similarity theory and $\Phi_m$ corresponds to the classic estimate used above.

Hence, we expect that the corrected coefficient $\beta_{\mathrm{m,cor}}$ matches better field observations where viscous effects are smaller than in our DNS.

Analogously, the viscous correction approach is applied on the stability function $\Phi_\mathrm{h}$ (11c) for buoyancy, with:

$$\Phi_{\mathrm{h,cor}}\left(\zeta_\mathrm{h}\right) = \Phi_\mathrm{h}\left(\zeta_\mathrm{h}\right) - \sqrt{\frac{\partial \langle b \rangle^+}{\partial z^+}} = \alpha_\mathrm{m} + \beta_{\mathrm{h,cor}} \zeta_\mathrm{h}. \tag{16b}$$

Our findings (Fig. 13) are in accordance with ( Chung and Matheou 2012, § 4.4); with decreasing Reynolds number and thus increasing stability (cf. $u_\star$ in Fig. 3a), a shift of the data to the left is observed.

For decreasing Reynolds numbers, the stability parameters $\beta_i$ are enhanced compared to the atmospheric value $\beta_i = 4.7$ (similar characteristic is observed in the study of Shah and Bou-Zeid 2014, ). Here, we measure $\beta_{\mathrm{m,cor}} = 4.88$ instead of $\beta_\mathrm{m} = 5.31$ (Fig. 10a) and $\beta_{\mathrm{h,cor}} = 11.7$ instead of $\beta_\mathrm{m} = 12.51$ (Fig. 10b). The relative importance of the viscous correction term in the regime $\zeta_i < 0.1$ is up to approximately 25 %. Near surface data of the *corrected* stability functions $\Phi_{i,\mathrm{cor}}$ for the cases `S064-S256P` reveal a better collapse of data with the weakly stable cases (grey to black data points in Fig. 13), observable in the region $0.04 \lesssim \zeta_i \lesssim 0.08$.

Högström (1988) proposed a second-order regression for the weakly stable regime ($\zeta_i \ll 1$) up to a threshold $\zeta_i = \zeta_{i,1}$ ($\zeta_{\mathrm{m},1} = 0.15$ and $\zeta_{\mathrm{h},1} = 0.2$), above which the common linear regression (12a) is valid. This approach improves the fit in the region $\zeta_i < 0.1$, since the linear regression systematically overestimates the data (Fig. 13). The best quadratic fits based on the cases `S001-S064` in the region $z^+_{\mathrm{log},i} \le z^+ \le 0.1 Re_\tau$ are:

$$\Phi_\mathrm{m}(\zeta_\mathrm{m}) - \alpha_\mathrm{m} = 2.41\zeta_\mathrm{m} + 16.48\zeta_\mathrm{m}^2, \tag{17a}$$

$$\Phi_\mathrm{h}(\zeta_\mathrm{h}) - \alpha_\mathrm{h} = 4.66\zeta_\mathrm{h} + 55.84\zeta_\mathrm{h}^2. \tag{17b}$$

We observe a larger scatter and stronger curvature of the data to the left for $\Phi_\mathrm{h}$ (cf. Figures 10b, 13b) compared to $\Phi_\mathrm{m}$ (Fig. 13b) and hence, estimate a large quadratic term which deviates

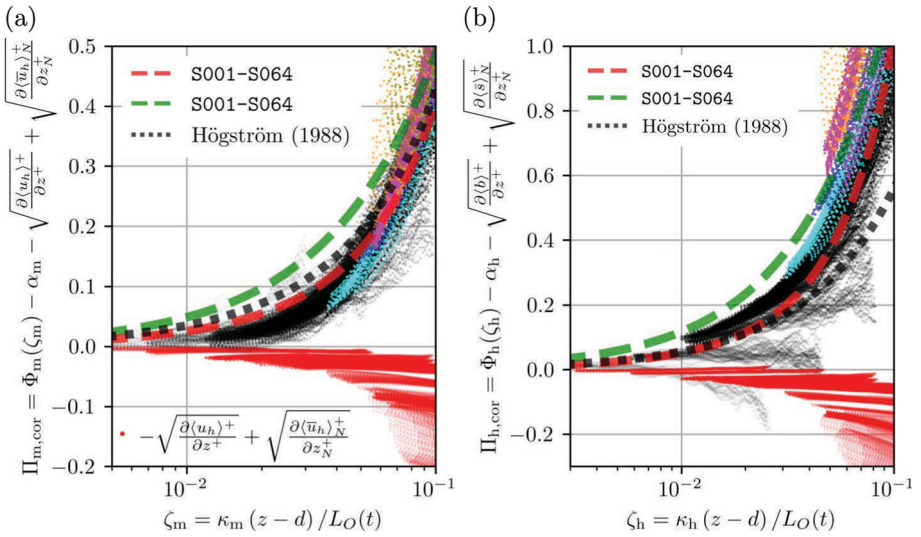


**Fig. 13** Similar to Fig. 10, with the viscous correction (magnitude of the correction depicted with red data points) with $\Pi_{i,\mathrm{cor}} = \Phi_{i,\mathrm{cor}}(\zeta_i) - \alpha_i$. Only the weakly stable regime is shown for $\zeta_i < 0.1$. Nevertheless, the regression lines (green and red dashed lines) are computed for $z^+ < 0.1\delta_\star$. **a** Lines: `S001-S064`, $\Phi_\mathrm{m} - \alpha_\mathrm{m} = 2.41\zeta_\mathrm{m} + 16.48\zeta_\mathrm{m}^2$ with $r^2 = 0.948$ (red dashed line); `S001-S064`, $\Phi_\mathrm{m} - \alpha_\mathrm{m} = 4.88\zeta_\mathrm{m}$ with $r^2 = 0.865$ (green dashed line); Högström (1988), $\Phi_\mathrm{m} - 1 = 3.43\zeta_\mathrm{m} + 8.4\zeta_\mathrm{m}^2$ (black dotted line). **b** Lines: `S001-S064`, $\Phi_\mathrm{h} - \alpha_\mathrm{h} = 4.66\zeta_\mathrm{h} + 55.84\zeta_\mathrm{h}^2$ with $r^2 = 0.929$ (red dashed line); `S001-S064`, $\Phi_\mathrm{h} - \alpha_\mathrm{h} = 11.7\zeta_\mathrm{h}$ with $r^2 = 0.818$ (green dashed line); Högström (1988), $\Phi_\mathrm{h} - 0.95 = 5.24\zeta_\mathrm{h} + 6.3\zeta_\mathrm{h}^2$ (black dotted line)

from the fits in the literature. In comparison, the quadratic fits according to Högström (1988) are $\Phi_\mathrm{m} - (1 \pm 0.018) = (3.34 \pm 0.32)\zeta + (8.4 \pm 5.9)\zeta^2$ and $\Phi_\mathrm{h} - (0.95 \pm 0.039) = (5.24 \pm 0.64)\zeta + (6.3 \pm 11.8)\zeta^2$, with standard error estimates (for $\zeta_i \leq 0.1$). In their study, they claim that the data base for $\Phi_\mathrm{h}$ is also less clear.

### 4.4 Dependence of the Richardson and Turbulent Prandtl Numbers on Stability

The Richardson flux and gradient numbers $Ri_f$ and $Ri_g$ (10) are, in addition to the Monin–Obukhov stability parameter $\zeta_i$, decisive measures of the flow stability and can be defined as (Stull 1988; Coleman et al. 1992):

$$Ri_f = \frac{\langle w'b' \rangle}{\langle u'w' \rangle \left(\partial \langle u \rangle / \partial z\right) + \langle v'w' \rangle \left(\partial \langle v \rangle / \partial z\right)} = \frac{\zeta_\mathrm{m}}{\Phi_\mathrm{m}}, \tag{18a}$$

$$Ri_g = \frac{\zeta_\mathrm{m}\Phi_\mathrm{h}}{\Phi_\mathrm{m}^2}, \tag{18b}$$

where $Ri_g = N^2/S^2$ is the ratio of the buoyancy, respectively the Brunt–Väi -sä -lä frequency $N$ and the shear frequency $S$. The Richardson flux number is the ratio of the TKE destruction (production) by buoyancy to the TKE production by shear and is a key parameter for turbulence closure schemes (cf. Mellor and Yamada 1974, 1982, ). The ratio of Richardson

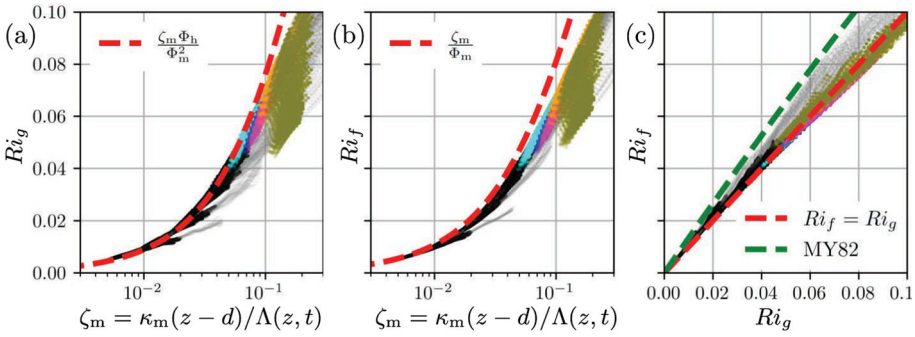


**Fig. 14** **a**, **b** The gradient and flux Richardson numbers $Ri_g(\zeta_m)$, $Ri_f(\zeta_m)$ as functions of the local stability parameter $\zeta_m$ and (c) the Richardson flux number $Ri_f(Ri_g)$. The parameters of the stability functions $\Phi_i$ in (**a**, **b**) from Fig. 11, the green curve in (**c**) after Mellor and Yamada (1974, 1982) (MY82) with $Ri_f = 0.725\left[Ri_g + 0.186 - \left(Ri_g^2 - 0.316Ri_g + 0.0346\right)^{1/2}\right]$. The coloured data is plotted within the constant-flux layer located in the region between the peak of the total turbulent flux $max\{\sqrt{\langle u'w'\rangle^2 + \langle v'w'\rangle^2}\}$ and where the flux is reduced by 10 % (Stull 1988). Light grey data in is plotted in the region $z^+_{\mathrm{log},i} \leq z^+ \leq 0.1Re_\tau$

numbers $Ri_g/Ri_f$ forms the turbulent Prandtl number $Pr_t$, given by:

$$Pr_t = \frac{Ri_g}{Ri_f} = \frac{(\partial\langle b\rangle/\partial z)\left[\langle u'w'\rangle\,(\partial\langle u\rangle/\partial z) + \langle v'w'\rangle\,(\partial\langle v\rangle/\partial z)\right]}{\langle w'b'\rangle\left[(\partial\langle u\rangle/\partial z)^2 + (\partial\langle v\rangle/\partial z)^2\right]} = \frac{\Phi_h}{\Phi_m} = \frac{\widetilde{K}_{\star,m}}{K_{\star,h}}. \quad (19)$$

The turbulent Prandtl number $Pr_t$ describes the difference in eddy viscosity $\widetilde{K}_{\star,m}$ and diffusivity $K_{\star,h}$, i.e. the difference in turbulent mixing of momentum and heat (cf. review by Li 2019, ). In (19), we follow the approach of Coleman et al. (1992) for $\widetilde{K}_{\star,m}$ which differs from the previous definition of $K_{\star,m}$ in (15c). We define the dimensionless numbers (18, 19) by considering the veering of the wind (coordinate system rotation) within the surface layer, since the lateral $v$-velocity component is nonzero for an Ekman flow.

The Richardson numbers in Fig. 14a, b increase with the stability parameter $\zeta_m$ and follow the proposed scaling approaches (red dashed lines), while a systematic shift of the data to the right is observed at higher stabilities.

This overestimation of $Ri_g$, $Ri_f$ is assumed to originate from the deviation of the linear stability functions and data in Fig. 11 at large $\zeta_i$. Within the considered regime $Ri_g \leq 0.1$, the dependence of $Ri_f(Ri_g)$ is linear ($\mathcal{O}(Ri_f/Ri_g) = 1$, cf. Figure 14c). The linear dependence of $Ri_f(Ri_g)$ for small $\zeta_m$ is in agreement with previous studies, e.g. Pardyjak et al. (2002) reports an increase of $Ri_f$ with $Ri_g$ until $Ri_g \approx 1$ and subsequently a levelling-off of $Ri_f$ with a maximum of approximately $0.4 - 0.5$ (cf. also Fig. 9, in Grachev et al. 2013, ). This characteristic can not be approved with our data, since the scatter of data is large outside the ASL for MOST. We observe an overestimation of $Ri_f$ by the parameterization of Mellor and Yamada (1974, 1982) of $\approx 20\,\%$.

The turbulent Prandtl number data as a function of the stability in the regime $z^+_{\mathrm{log},i} \leq z^+ \leq 0.1Re_\tau$ exhibits a large scatter (Fig. 15).

If the turbulent Prandtl number is considered in the constant-flux layer (validity region of MOST), or merely at the lower bound at $z^+ = 50$ where the vertical turbulent flux tends to peak (red data points in Fig. 15), $Pr_t$ increases with stability (similar for $Pr_t(Ri_f)$, not shown here) with a neutral value of $Pr_{t,0} = Pr_t|_{Ri_g=0} \approx 0.94$ and hence, the surface-layer

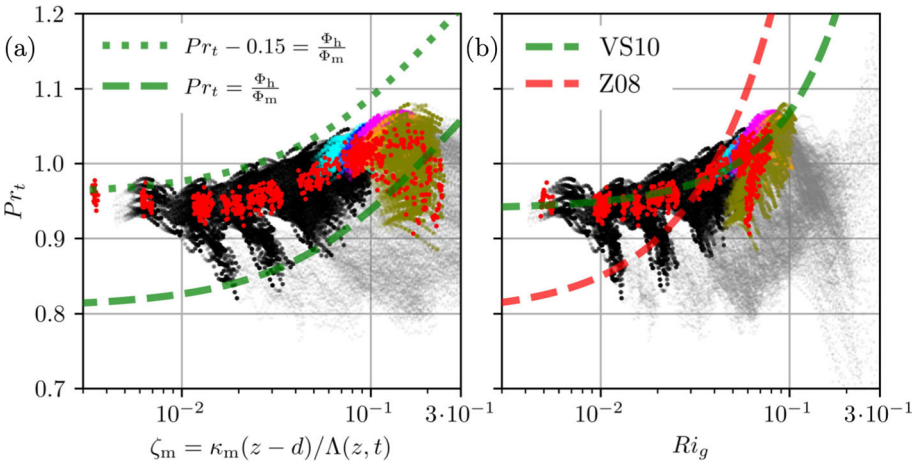


**Fig. 15** **a** Turbulent Prandtl number $Pr_t(\zeta_m)$, with the parameters of the stability functions $\Phi_i$ from Fig. 11. **b** $Pr_t(Ri_g)$ vs. stability ($Ri_\Lambda$), with the fit (green line) based on (20) (cf. Equation 3.6, Venayagamoorthy and Stretch 2010, (VS10)) and the fit (red line) based on (Zilitinkevich et al. (2008), (Z08)) with $Pr_t = 0.8 + 5Ri_g$. The data shown here is similar to Fig. 14 and red data points are located at $z^+ = 50$

data is located between the envelopes $Pr_t = \Phi_h/\Phi_m$ and $Pr_t - 0.15 = \Phi_h/\Phi_m$ (Fig. 15a). The $Pr_t(Ri_g)$ model of Venayagamoorthy and Stretch (2010) (their Eq. 3.6), which is refined from Schumann and Gerz (1995) (their Eq. 22), takes the form of:

$$Pr_t = Pr_{t,0} \exp\left(-\frac{Ri_g}{Pr_{t,0} Ri_{f,\infty}} + \frac{Ri_g}{Pr_{t,0}}\right) + \frac{Ri_g}{Ri_{f,\infty}}, \tag{20}$$

with $Ri_{f,\infty} = Ri_f\big|_{Ri_g=\infty}$. The model (20) shows surprisingly good agreement with our data (Fig. 15b), with $Pr_{t,0} = \lim_{Ri_g \to 0} Pr_t(Ri_g) = 0.15 + \alpha_h/\alpha_m \approx 0.94$ and $Ri_{f,\infty} = \lim_{Ri_g \to \infty} Ri_f(Ri_g) = \beta_m^{-1} \approx 0.29$. Further, Zilitinkevich et al. (2008) propose the relation $Pr_t \approx Pr_{t,0} + 5Ri_g$, with the asymptote $Pr_{t,0} \approx 0.8$, based on measurement campaigns, experimental and modelling results. In contrast to the previous model (20) this overestimates our data for large $Ri_g$, and underestimates for small $Ri_g$. The increasing behaviour of $Pr_t$ with increasing stability is supported by the findings of Mauritsen and Svensson (2007), where they find finite values of the momentum flux and zero values of the heat flux for $Ri_g \gg 1$. The asymptotical behaviour of $Pr_t$ for small $\zeta$ is $Pr_{t,0} \sim \alpha_h/\alpha_m$ (*z-less* stratification, Wyngaard 1973) and therefore, 0.74 for Businger et al. (1971) and 1.0 for Dyer (1974). Townsend (1976); Yakhot and Orszag (1986) predict a neutral value of $\approx 0.7$ and Schumann and Gerz (1995) expect values between 0.7 and 1.2. The asymptotical value of $Ri_{f,\infty}$ is according to Nieuwstadt (1984) 0.2 and Schumann and Gerz (1995) 0.25 and hence, our values of $Pr_{t,0}$, $Ri_{f,\infty}$ fit well with those of the literature.

The dependence of the Prandtl number in the stable regime is controversial. A major challenge, apart from the large scatter of measurement data, is self-correlation of $Pr_t$ with the stability measures, due to shared variables (e.g. velocity and buoyancy gradients are present in $Pr_t$ and $Ri_g$, cf. discussions in Grachev et al. (2007); Mahrt (2007); Anderson (2009); Sorbjan and Grachev (2010). Mahrt (2007) points out the importance of non-stationarity in the VSBL, where non-turbulent motions (e.g. wave-like, meandering motions) transport

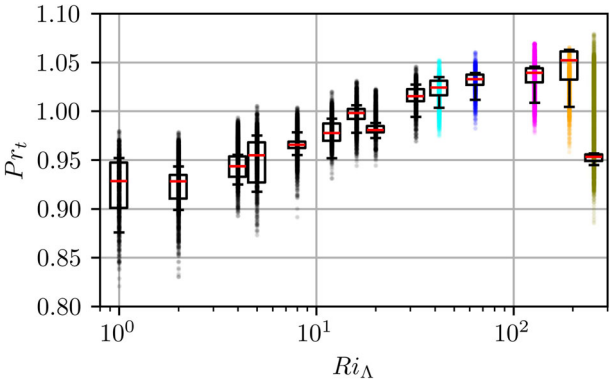


**Fig. 16** The turbulent Prandtl number $Pr_t(Ri_\Lambda)$ as a function of the external stability parameter $Ri_\Lambda$ (4c). The data points are in the constant-flux layer and the box plots are derived from the data shown here

momentum more efficiently than heat, suggesting an increase of the turbulent Prandtl number with stability. This behaviour is supported by the ratio $Ri_g/Ri_f$, since $Ri_f$ is assumed to reach a constant, whereas $Ri_g$ increases. Howell and Sun (1999) observed $Pr_t(\zeta) \approx 1.0$ for $10^{-2} < \zeta < 10^1$, with a large scatter in the data similar to Yagüe et al. (2001), where an exact dependence of $Pr_t$ on $\zeta$ remains uncertain. Whereas Yagüe et al. (2001) reports an increase of $Pr_t(Ri_g)$ at $Ri_g \gtrsim 0.1$. Sorbjan and Grachev (2010) found a neutral value $Pr_{t,0} = 0.9$ and a slight decrease with $Ri_g$ to 0.7, after neglecting outliers in $Ri_g$ from the analysis.

To circumvent self-correlation, Grachev et al. (2007) considers the $Pr_t$ as a function of the Richardson bulk number $Ri_B$ (cf. their Eq. 6 for the bulk Richardson number $Ri_B$) and finds a decrease with stability. Anderson (2009) proposed a self-correlation free method and observes an increase of the Prandtl number as a function of the gradient Richardson number $Pr_t(Ri_g)$. In our simulations, the turbulent Prandtl number $Pr_t(Ri_\Lambda)$ in the surfaces layer increases as a function of the external Richardson number $Ri_\Lambda$ (4c, Fig. 16), contrasting the results of Grachev et al. (2007).

While the data for $Pr_t$ presented in this study (Figs. 15, 16) exhibit a substantial scatter, we find that $Pr_t$ increases in the constant-flux layer with any of the stability measures $Ri_g$, $Ri_f$, $\zeta_\mathrm{m}$, $Ri_\Lambda$. The most stable, intermittently turbulent case `S256P` shows a different behaviour, which is related to the large imbalance in TKE; in fact, this case features such a thin boundary layer that it is not possible to identify a surface layer by strict criteria.

## 5 Discussion and Conclusions

We investigate the competing interaction of small-scale surface roughness and stable stratification on ASL similarity using idealized DNS of turbulent Ekman flow. The surface roughness is fully resolved with an immersed boundary method (ADR IBM) and the flow is driven with an identical large-scale forcing for all cases. On the lower boundary there are $56 \times 56$ rectangular blocks with a certain degree of randomness in structure and layout, which leaves the setup under neutral stratification on the verge of the transitionally to fully rough regime, with $z_0^+ \approx 2$. The stability of the flow is incrementally increased in 12 steps to cover the full span of the stability regime, from the WSBL to the VSBL at meaningful scale separation (high

Reynolds number in DNS context, $Re_{\tau,N} \approx 2700$, $Re_D = 1000$). We now conclude with respect to the research questions posed in Sect. 1.

(1) *The presence of small-scale surface roughness extends the stability regime, where turbulence is in a continuous state.* Roughness is observed to be a very effective triggering mechanism of turbulence by inducing flow instabilities, since flow around objects with sharp edges creates detached eddies and turbulent mixing. This enhances the production of TKE in the ASL and counteracts the suppression of turbulence by buoyancy. The WSBL regime is extended, which is characterized by a decreasing boundary layer depth and a continuous state of turbulence. This gives rise to a pronounced plateau of the vertically integrated buoyancy flux (MSHF concept) over an extensive stability regime. The regime transition from the WSBL to the VSBL manifests itself in distinct oscillations of global flow properties with decaying amplitude in time, such as $u_\star$ and $L_O^+$. At the transition to the VSBL, where a drastic decrease of turbulence is observable, buoyancy is dominating with $L_O \lesssim \delta_{95}$, $Ri_{B,95} \approx 1$ and where $L_O^+$ gets close to $Re_{L,\mathrm{crit}}$.

(2) *Global intermittency is an inherent characteristic of the rough VSBL.* In the presence of surface roughness, global intermittency in the VSBL is successfully simulated and observed to appear in space (across the boundary layer) and time (oscillating intensity). In this study, it was not possible to completely laminarize the flow at very strong stability. We therefore assume that the intermittency in the VSBL over heterogeneous surfaces lasts over a broader stability range than in the VSBL over smooth surfaces, where complete laminarization of the flow occurs for smaller values of stable stratification. This is supported by observation of intermittency in the real-world SBL, since the atmospheric Reynolds number is large, the Earth's surface is rough and hence, a complete laminarization is not observed. Here, further investigation would shed light on the intermittency phenomenon over rough surfaces.

(3) *Turning of the wind is enhanced in the rough VSBL and an appropriate boundary layer depth scale is* $\delta_{\star,95}$. The turning of the surface wind with respect to the geostrophic wind is enhanced by roughness. In the VSBL values of $\alpha_\star > 90°$ are observed for case `S256P`, which exceeds by far the laminar limit of $\alpha_\star = 45°$ for an Ekman flow. The proposed mechanism is based on the momentum balance within the surface roughness. With increasing stability, the velocity is reduced and so are the Coriolis and friction force. Eventually, the wind turns in favour of the pressure gradient force, resulting in a large $\alpha_\star$, which we suggest as the reason for pressure-driven channeling in more complex situations. With increasing stratification, the boundary layer thickness decreases: When comparing the neutral case `N` and the very stable case `S256P`, $\delta_\star$ is reduced by approximately 30 %, $\delta_{\star,95}$ by 90 %, which changes their ratio from $\delta_{\star,95}/\delta_\star \approx 0.55$ in the neutral regime to $\approx 0.08$ in the VSBL. Both visual inspection of the flow and scaling of global stability measures, such as $Ri_{B,95}$, $L_O/\delta_{95}$ suggest that the boundary layer depth $\delta_{\star,95}$ is an appropriate scale in case of stable stratification rather than the scale $\delta_\star$.

(4) *Surface layer similarity holds in the known limits for the cases* `S001-S064`. With the displacement height $d/H = 2/3$, von Kármán constants of heat and momentum $\kappa_\mathrm{m} = 0.42$, $\kappa_\mathrm{h} = 0.35$, we estimate the following parameters of the linear MOST correction functions: $\alpha_\mathrm{m} = 0.89$, $\alpha_\mathrm{h} = 0.72$ and $\beta_\mathrm{m} = 5.3$, $\beta_\mathrm{h} = 12.5$. In contrast to classical MOST, local similarity theory results in a more accurate collapse of the data onto the linear fit, with slope parameters of $\beta_\mathrm{m} = 3.45$, $\beta_\mathrm{h} = 5.21$. For large stability values, we observe a levelling-off of the stability correction, which is in accordance with observations. Viscous effects impact ASL theory, due to the present intermediate Reynolds number compared to the atmospheric one. Hence, we propose a viscous correction method for the MOST and reveal, that fitting parameters converge closer to the observational values. Furthermore, based on the current data, we observe that a linear stability correction function is overestimating for small and

underestimating for large stabilities ($\zeta$). Here, a quadratic fit in the WSBL regime seems to improve the collapse of data, in agreement with the fits derived by Högström (1996) based on observational data.

Regarding the controversial discussion on the turbulent Prandtl number $Pr_t$ and its dependence on stability (e.g. $\zeta$, $Ri_f$, $Ri_g$), –despite substantial scatter–we observe an increase with stability and a neutral value of $Pr_{t,0} \approx 0.94$.

In summary, we provide a setup consistently treating outer dynamics in the boundary layer (i.e. the rotation, and associated triadic balance in Ekman flow), the turbulent mixing in the logarithmic layer and the immediate interaction with the surface through a roughness layer and viscous sublayer. While this requires substantial numerical resources on the largest supercomputers, it yields valuable insight to the boundary-layer dynamics. Based on an analysis of well-known surface-layer scaling relations, we show that roughness helps to maintain turbulence and shifts the stability regimes to higher stratification (cf. 1), that global intermittency is an intrinsic characteristic, also of the rough boundary layer (cf. 2), that stratification and roughness together can cause over-veering of the wind (cf. 3). The agreement of results from such a strongly idealized setup with MOST and the semi-empirical fits based on field observation demonstrates the consistency of our setup and its relevance for atmospheric conditions when the data is scaled properly. Indeed, the results underline the potential of such idealized setup to further address open questions regarding land–atmosphere interactions on the process-level, for the first time also including processes in the roughness sublayer.

## Appendix 1: Determination of the Stability Functions for Neutral Stratification

The linear stability correction functions (12a) reduce to $\Phi_i|_{\zeta_i=0} = \alpha_i$ at neutral stratification. Based on theory, the empirical parameter for momentum $\alpha_\mathrm{m}$ is equal to unity in order to retain the logarithmic law of the wall for the mean velocity. For buoyancy, the parameter $\alpha_\mathrm{h}$ equals the ratio of the von Kármán constants of heat and momentum $\alpha_\mathrm{h} = \kappa_\mathrm{h}/\kappa_\mathrm{m}$ (Brutsaert 1982; Chenge and Brutsaert 2005), or it is interpreted as $\alpha_\mathrm{h} = \alpha_\mathrm{m}/(K_\mathrm{h}/K_\mathrm{m})$, depending on the ratio of the eddy diffusivities $K_\mathrm{h}$, $K_\mathrm{m}$. For momentum, the common value in the literature is $\alpha_\mathrm{m} = 1$, while the picture is less clear for buoyancy. Chenge and Brutsaert (2005) proposed equal values for the von Kármán constants and therefore $\alpha_\mathrm{h} = 1$ (the so-called Reynolds analogy, namely equal transport properties for heat and momentum), Businger et al. (1971) give $\alpha_\mathrm{h} = 0.74$ and Högström (1988) gives $\alpha_\mathrm{h} = 0.95$. However, Businger et al. (1971) corrected the value of the commonly accepted von Kármán constant $\kappa_\mathrm{m} = 0.4$ to $\kappa_\mathrm{m} = 0.35$ to obtain $\alpha_\mathrm{m} = 1$ instead of $\alpha_\mathrm{m} = 1.15$ and used $\kappa_\mathrm{m} = \kappa_\mathrm{h}$ and argued that the eddy diffusivities are different for heat and momentum.

The empirical slope parameters $\beta_i$ from Sect. 4.1 with $\beta_\mathrm{m} = 5.31$, $\beta_\mathrm{h} = 12.51$ are taken to estimate the parameters $\alpha_i$ with a least squares fit within the constant-flux layer for the cases `S001-S064`, where MOST is valid (cf. Fig. 17).

With this approach, we estimate $\alpha_\mathrm{h} = 0.72$, which is similar to the common literature value, and $\alpha_\mathrm{m} = 0.89$, which does not fit the expected value of unity.

Here, we do not follow the approach by Businger et al. (1971) to correct the von Kármán constants to gain $\alpha_\mathrm{m} = 1$. We take the carefully estimated values of the von Kármán constants from KA24 at neutral stratification, namely $\kappa_\mathrm{m} = 0.42$, $\kappa_\mathrm{h} = 0.35$ and assume that these are universal, since the flow type is unchanged between the current study and KA24. The

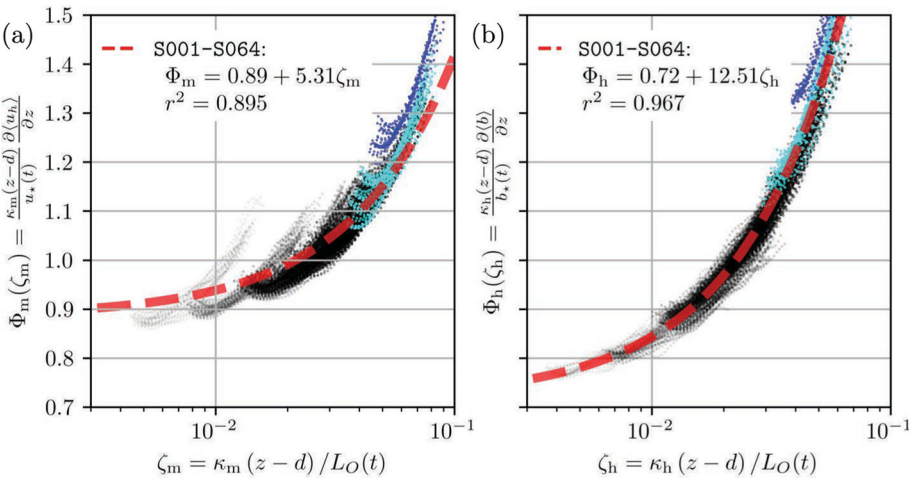


**Fig. 17** Stability correction functions $\Phi_i(\zeta_i)$ for the cases `S001-S064`. The data is plotted within the constant-flux layer located in the region between the peak of the total turbulent flux $max\{\sqrt{\langle u'w'\rangle^2 + \langle v'w'\rangle^2}\}$ and where the flux is reduced by 10 % (Stull 1988). The linear regression lines (red dashed lines) are derived with the slope parameters $\beta_i$ from Sect. 4.1

analysis concerning the MOST in the current study is exempted from the precise values of $\alpha_i$ through removing the neutral share of the dimensionless gradients.

**Acknowledgements** We are grateful for the invaluable insights provided by Prof. B. J. H. van de Wiel and two anonymous reviewers, which shaped and improved this article. Simulations were performed on the resources of the High-Performance Computing Center Stuttgart (HLRS) on the `Hawk` cluster, founded by the Baden–Württemberg Ministry of Science, Research, and the Arts and the German Federal Ministry of Education and Research through the Gauss Centre for Supercomputing. The computing time and storage facilities were provided by the project 'trainABL' (ACID 44187). We further acknowledge the support of FU Berlin's refubium team in the process of data publication.

**Author Contributions** J.K. conducted the numerical simulations, performed the post-processing of the data, created the visualizations, interpreted the results and wrote the original draft. Both authors contributed to the conceptualization of the study. C.A. supervised the research, contributed with discussion and interpretation of results, reviewed and edited the original draft and was responsible for acquisition of funding.

**Funding** Open Access funding enabled and organized by Projekt DEAL. The authors acknowledge financial support through the ERC grant trainABL with the project number 851374; https://doi.org/10.3030/851374.

**Data availability** The data supporting the findings of this study is published under the F.A.I.R. paradigm (cf. *open access*) in Kostelecky and Ansorge (2024b).

## Declarations

**Conflict of interest** The authors declare no Conflict of interest.

## References

Adrian RJ (2007) Hairpin vortex organization in wall turbulence. Phys Fluids 19(4):041301. https://doi.org/10.1063/1.2717527

Anderson PS (2009) Measurement of Prandtl number as a function of Richardson number avoiding self-correlation. Boundary-Layer Meteorol 131(3):345–362. https://doi.org/10.1007/s10546-009-9376-4

Ansorge C (2019) Scale dependence of atmosphere-surface coupling through similarity theory. Boundary-Layer Meteorol 170(1):1–27. https://doi.org/10.1007/s10546-018-0386-y

Ansorge C, Mellado JP (2014) Global intermittency and collapsing turbulence in the stratified planetary boundary layer. Boundary-Layer Meteorol 153(1):89–116. https://doi.org/10.1007/s10546-014-9941-3

Ansorge C, Mellado JP (2016) Analyses of external and global intermittency in the logarithmic layer of Ekman flow. J Fluid Mech 805:611–635. https://doi.org/10.1017/jfm.2016.534

Atoufi A, Scott KA, Waite ML (2021) Kinetic energy cascade in stably stratified open-channel flows. J Fluid Mech 925:A25. https://doi.org/10.1017/jfm.2021.665

Bhimireddy SR, Sun J, Wang J, Kristovich DAR, Hiscox AL (2024) Effect of small-scale topographical variations and fetch from roughness elements on the stable boundary layer turbulence statistics. Boundary-Layer Meteorol 190(1):1–19. https://doi.org/10.1007/s10546-023-00855-5

Bon T, Cal RB, Meyers J (2024) Stable boundary layers with subsidence: scaling and similarity of the steady state. Boundary-Layer Meteorol 190(10):42. https://doi.org/10.1007/s10546-024-00882-w

Boyko V, Vercauteren N (2024) Simulating the unsteady stable boundary layer with a stochastic stability equation. J Geophys Res Atmos 129(5):e2023JD039370. https://doi.org/10.1029/2023JD039370

Brutsaert W (1982) Evaporation into the atmosphere. Springer, Netherlands. https://doi.org/10.1007/978-94-017-1497-6

Businger JA (1973) Turbulence transfer in the atmospheric surface layer. American Meteorological Society, Workshop on Micrometeorology

Businger JA, Wyngaard JC, Izumi Y, Bradley EF (1971) Flux-profile relationships in the atmospheric surface layer. J Atmos Sci 28(2):181–189. https://doi.org/10.1175/1520-0469(1971)028%3C0181:FPRITA%3E2.0.CO;2

Chenge Y, Brutsaert W (2005) Flux-profile relationships for wind speed and temperature in the stable atmospheric boundary layer. Boundary-Layer Meteorol 114(3):519–538. https://doi.org/10.1007/s10546-004-1425-4

Chinita MJ, Matheou G, Miranda PMA (2022) Large-eddy simulation of very stable boundary layers. Part I: modeling methodology. Q J R Meteorol Soc 148(745):1805–1823. https://doi.org/10.1002/qj.4279

Chung D, Matheou G (2012) Direct numerical simulation of stationary homogeneous stratified sheared turbulence. J Fluid Mech 696:434–467. https://doi.org/10.1017/jfm.2012.59

Coleman GN (1999) Similarity statistics from a direct numerical simulation of the neutrally stratified planetary boundary layer. J Atmos Sci 56(6):891–900. https://doi.org/10.1175/1520-0469(1999)056%3C0891:SSFADN%3E2.0.CO;2

Coleman GN, Ferziger JH, Spalart PR (1990) A numerical study of the turbulent Ekman layer. J Fluid Mech 213:313–348. https://doi.org/10.1017/S0022112090002348

Coleman GN, Ferziger JH, Spalart PR (1992) Direct simulation of the stably stratified turbulent Ekman layer. J Fluid Mech 244:677–712. https://doi.org/10.1017/S0022112092003264

De Bruin HAR (1994) Analytic solutions of the equations governing the temperature fluctuation method. Boundary-Layer Meteorol 68(4):427–432. https://doi.org/10.1007/BF00706800

Deusebio E, Brethouwer G, Schlatter P, Lindborg E (2014) A numerical study of the unstratified and stratified Ekman layer. J Fluid Mech 755:672–704. https://doi.org/10.1017/jfm.2014.318

Deusebio E, Caulfield CP, Taylor JR (2015) The intermittency boundary in stratified plane Couette flow. J Fluid Mech 781:298–329. https://doi.org/10.1017/jfm.2015.497

Donda JMM, van Hooijdonk IGS, Moene AF, Jonker HJJ, van Heijst GJF, Clercx HJH, van de Wiel BJH (2015) Collapse of turbulence in stably stratified channel flow: a transient phenomenon. Q J R Meteorol Soc 141(691):2137–2147. https://doi.org/10.1002/qj.2511

Donda JMM, van Hooijdonk IGS, Moene AF, van Heijst GJF, Clercx HJH, van de Wiel BJH (2016) The maximum sustainable heat flux in stably stratified channel flows. Q J R Meteorol Soc 142(695):781–792. https://doi.org/10.1002/qj.2680

Dyer AJ (1974) A review of flux-profile relationships. Boundary-Layer Meteorol 7(3):363–372. https://doi.org/10.1007/BF00240838

Edwards JM, Beljaars ACM, Holtslag AAM, Lock AP (2020) Representation of boundary-layer processes in numerical weather prediction and climate models. Boundary-Layer Meteorol 177(2):511–539. https://doi.org/10.1007/s10546-020-00530-z

Ekman VW (1905) On the influence of the earth's rotation on ocean-currents. Arkiv for Matematik, Astronomi Och Fysik 2:1–53

Fiedler F (1983) Einige Charakteristika der Strömung im Oberrheingraben. Wissenschaftliche Berichte des Instituts für Meteorologie und Klimaforschung der Universität Karlsruhe 4:113–123

Flores O, Riley JJ (2011) Analysis of turbulence collapse in the stably stratified surface layer using direct numerical simulation. Boundary-Layer Meteorol 139(2):241–259. https://doi.org/10.1007/s10546-011-9588-2

Foken T (2006) 50 years of the Monin–Obukhov similarity theory. Boundary-Layer Meteorol 119(3):431–447. https://doi.org/10.1007/s10546-006-9048-6

García-Villalba M, del Álamo JC (2011) Turbulence modification by stable stratification in channel flow. Phys Fluids 23(4):1–22. https://doi.org/10.1063/1.3560359

Garg RP, Ferziger JH, Monismith SG, Koseff JR (2000) Stably stratified turbulent channel flows. I. Stratification regimes and turbulence suppression mechanism. Phys Fluids 12(10):2569–2594. https://doi.org/10.1063/1.1288608

Garratt JR (1992) The Atmospheric boundary layer. Cambridge atmospheric and space science series, Cambridge University Press, Cambridge

Giannenas AE, Laizet S (2021) A simple and scalable immersed boundary method for high-fidelity simulations of fixed and moving objects on a Cartesian mesh. Appl Math Model 99:606–627. https://doi.org/10.1016/j.apm.2021.06.026

Grachev AA, Andreas EL, Fairall CW, Guest PS, Persson POG (2007) On the turbulent Prandtl number in the stable atmospheric boundary layer. Boundary-Layer Meteorol 125(2):329–341. https://doi.org/10.1007/s10546-007-9192-7

Grachev AA, Andreas EL, Fairall CW, Guest PS, Persson POG (2013) The critical Richardson number and limits of applicability of local similarity theory in the stable boundary layer. Boundary-Layer Meteorol 147(1):51–82. https://doi.org/10.1007/s10546-012-9771-0

Grimmond CSB, Oke TR (1999) Aerodynamic properties of urban areas derived from analysis of surface form. J Appl Meteorol Climatol 38(9):1262–1292. https://doi.org/10.1175/1520-0450(1999)038%3C1262:APOUAD%3E2.0.CO;2

Gucci F, Giovannini L, Stiperski I, Zardi D, Vercauteren N (2023) Sources of anisotropy in the Reynolds stress tensor in the stable boundary layer. Q J R Meteorol Soc 149(750):277–299. https://doi.org/10.1002/qj.4407

Högström U (1988) Non-dimensional wind and temperature profiles in the atmospheric surface layer: a re-evaluation. Boundary-Layer Meteorol 42(1):55–78. https://doi.org/10.1007/BF00119875

Högström U (1996) Review of some basic characteristics of the atmospheric surface layer. Boundary-Layer Meteorol 78(3):215–246. https://doi.org/10.1007/BF00120937

Holtslag AAM, Svensson G, Baas P, Basu S, Beare B, Beljaars ACM, Bosveld FC, Cuxart J, Lindvall J, Steeneveld GJ, Tjernström M, Van de Wiel BJH (2013) Stable atmospheric boundary layers and diurnal cycles: challenges for weather and climate models. Bull Am Meteor Soc 94(11):1691–1706. https://doi.org/10.1175/BAMS-D-11-00187.1

Howell JF, Sun J (1999) Surface-layer fluxes in stable conditions. Boundary-Layer Meteorol 90(3):495–520. https://doi.org/10.1023/A:1001788515355

Jiménez MA, Cuxart J (2005) Large-eddy simulations of the stable boundary layer using the standard Kolmogorov theory: range of applicability. Boundary-Layer Meteorol 115(2):241–261. https://doi.org/10.1007/s10546-004-3470-4

Kalthoff N, Vogel B (1992) Counter-current and channelling effect under stable stratification in the area of Karlsruhe. Theoret Appl Climatol 45(2):113–126. https://doi.org/10.1007/BF00866400

Kosović B, Curry JA (2000) A large eddy simulation study of a quasi-steady, stably stratified atmospheric boundary layer. J Atmos Sci 57(8):1052–1068. https://doi.org/10.1175/1520-0469(2000)057%3C1052:ALESSO%3E2.0.CO;2

Kostelecky J, Ansorge C (2024a) Simulation and scaling analysis of periodic surfaces with small-scale roughness in turbulent Ekman flow. J Fluid Mech 992:A8. https://doi.org/10.1017/jfm.2024.542
Kostelecky J, Ansorge C (2024b) Turbulent Ekman flow with cubic small-scale surface roughness under stable stratification (Re=1000). https://doi.org/10.17169/refubium-45292
Lee S, Gohari SMI, Sarkar S (2020) Direct numerical simulation of stratified Ekman layers over a periodic rough surface. J Fluid Mech 902:A25. https://doi.org/10.1017/jfm.2020.590
Lele SK (1992) Compact finite difference schemes with spectral-like resolution. J Comput Phys 103(1):16–42. https://doi.org/10.1016/0021-9991(92)90324-R
LeMone MA, Angevine WM, Bretherton CS, Chen F, Dudhia J, Fedorovich E, Katsaros KB, Lenschow DH, Mahrt L, Patton EG, Sun J, Tjernström M, Weil J (2019) 100 years of progress in boundary layer meteorology. Meteorol Monogr 59(1):9.1-9.85. https://doi.org/10.1175/AMSMONOGRAPHS-D-18-0013.1
Li D (2019) Turbulent Prandtl number in the atmospheric boundary layer-where are we now? Atmos Res 216:86–105. https://doi.org/10.1016/j.atmosres.2018.09.015
Mahrt L (1998) Stratified atmospheric boundary layers and breakdown of models. Theoret Comput Fluid Dyn 11(3):263–279. https://doi.org/10.1007/s001620050093
Mahrt L (1999) Stratified atmospheric boundary layers. Boundary-Layer Meteorol 90(3):375–396. https://doi.org/10.1023/A:1001765727956
Mahrt L (2007) The influence of nonstationarity on the turbulent flux-gradient relationship for stable stratification. Boundary-Layer Meteorol 125(2):245–264. https://doi.org/10.1007/s10546-007-9154-0
Mahrt L (2014) Stably stratified atmospheric boundary layers. Annu Rev Fluid Mech 46(1):23–45. https://doi.org/10.1146/annurev-fluid-010313-141354
Marlatt S, Waggy S, Biringen S (2012) Direct numerical simulation of the turbulent Ekman layer: evaluation of closure models. J Atmos Sci 69(3):1106–1117. https://doi.org/10.1175/JAS-D-11-0107.1
Maroneze R, Costa FD, Acevedo OC, Medeiros LE, Puhales FS, Anabor V, Mortarini L (2023) A new stable boundary layer parameterization for numerical weather prediction models: a heat flux budget approach. Boundary-Layer Meteorol 188(2):209–228. https://doi.org/10.1007/s10546-023-00810-4
Mauritsen T, Svensson G (2007) Observations of stably stratified shear-driven atmospheric turbulence at low and High Richardson numbers. J Atmos Sci 64(2):645–655. https://doi.org/10.1175/JAS3856.1
Mellado JP, Ansorge C (2012) Factorization of the Fourier transform of the pressure-Poisson equation using finite differences in colocated grids. ZAMM-J Appl Math Mech/Zeitschrift für Angewandte Mathematik und Mechanik 92(5):380–392. https://doi.org/10.1002/zamm.201100078
Mellado JP, Bretherton CS, Stevens B, Wyant MC (2018) DNS and LES for simulating stratocumulus: better together. J Adv Model Earth Syst 10(7):1421–1438. https://doi.org/10.1029/2018MS001312
Mellor GL, Yamada T (1974) A hierarchy of turbulence closure models for planetary boundary layers. J Atmos Sci 31(7):1791–1806. https://doi.org/10.1175/1520-0469(1974)031%3C1791:AHOTCM%3E2.0.CO;2
Mellor GL, Yamada T (1982) Development of a turbulence closure model for geophysical fluid problems. Rev Geophys 20(4):851–875. https://doi.org/10.1029/RG020i004p00851
Mironov DV, Sullivan PP (2023) Turbulence structure and mixing in strongly stable boundary-layer flows over thermally heterogeneous surfaces. Boundary-Layer Meteorol 187(1):371–393. https://doi.org/10.1007/s10546-022-00766-x
Miyashita K, Iwamoto K, Kawamura H (2006) Direct numerical simulation of the neutrally stratified turbulent Ekman boundary layer. J Earth Simul 6:3–15
Monin AS (1970) The atmospheric boundary layer. Annu Rev Fluid Mech 2(1):225–250. https://doi.org/10.1146/annurev.fl.02.010170.001301
Nieuwstadt FTM (1984) The turbulent structure of the stable, nocturnal boundary layer. J Atmos Sci 41(14):2202–2216. https://doi.org/10.1175/1520-0469(1984)041%3C2202:TTSOTS%3E2.0.CO;2
Nieuwstadt FTM (2005) Direct numerical simulation of stable channel flow at large stability. Boundary-Layer Meteorol 116(2):277–299. https://doi.org/10.1007/s10546-004-2818-0
Obukhov AM (1971) Turbulence in an atmosphere with a non-uniform temperature. Boundary-Layer Meteorol 2(1):7–29. https://doi.org/10.1007/BF00718085
Pardyjak ER, Monti P, Fernando HJS (2002) Flux Richardson number measurements in stable atmospheric shear flows. J Fluid Mech 459:307–316. https://doi.org/10.1017/S0022112002008406
Pope SB (2000) Turbulent flows. Cambridge University Press, Cambridge
Prandtl L (1925) 7. Bericht über Untersuchungen zur ausgebildeten Turbulenz. ZAMM-J Appl Math Mech/Zeitschrift für Angewandte Mathematik und Mechanik 5(2):136–139. https://doi.org/10.1002/zamm.19250050212
Rossby CG, Montgomery RB (1935) The layer of frictional influence in wind and ocean currents. Massachusetts Institute of Technology and Woods Hole Oceanographic Institution, Cambridge and Woods. https://doi.org/10.1575/1912/1157

Rotta JC (1972) Turbulente Strömungen: eine Einführung in die Theorie und ihre Anwendung. No. 15 in Leitfäden der angewandten Mathematik und Mechanik, Teubner, Stuttgart
Sandu I, Beljaars A, Bechtold P, Mauritsen T, Balsamo G (2013) Why is it so difficult to represent stably stratified conditions in numerical weather prediction (NWP) models? J Adv Model Earth Syst 5(2):117–133. https://doi.org/10.1002/jame.20013
Schumann U, Gerz T (1995) Turbulent mixing in stably stratified shear flows. J Appl Meteorol Climatol 34(1):33–48. https://doi.org/10.1175/1520-0450-34.1.33
Shah SK, Bou-Zeid E (2014) Direct numerical simulations of turbulent Ekman layers with increasing static stability: modifications to the bulk structure and second-order statistics. J Fluid Mech 760:494–539. https://doi.org/10.1017/jfm.2014.597
Shingai K, Kawamura H (2004) A study of turbulence structure and large-scale motion in the Ekman layer through direct numerical simulations. J Turbul 5(1):1–18. https://doi.org/10.1088/1468-5248/5/1/013
Sorbjan Z, Grachev AA (2010) An evaluation of the flux-gradient relationship in the stable boundary layer. Boundary-Layer Meteorol 135(3):385–405. https://doi.org/10.1007/s10546-010-9482-3
Spalart PR (1989) Theoretical and numerical study of a three-dimensional turbulent boundary layer. J Fluid Mech 205:319–340. https://doi.org/10.1017/S0022112089002053
Spalart PR, Coleman GN, Johnstone R (2008) Direct numerical simulation of the Ekman layer: a step in Reynolds number, and cautious support for a log law with a shifted origin. Phys Fluids 20(10):101507. https://doi.org/10.1063/1.3005858
Spalart PR, Coleman GN, Johnstone R (2009) Retraction: "Direct numerical simulation of the Ekman layer: a step in Reynolds number, and cautious support for a log law with a shifted origin" [Phys. Fluids 20, 101507 (2008)]. Phys Fluids 21(10):109901. https://doi.org/10.1063/1.3247176
Steeneveld GJ (2014) Current challenges in understanding and forecasting stable boundary layers over land and ice. Front Environ Sci 2(41):1–6. https://doi.org/10.3389/fenvs.2014.00041
Stefanello M, Frantz RAS, Acevedo O, Degrazia G, Silvestrini JH (2022) Horizontal meandering in direct numerical simulations of the stable boundary layer. Q J R Meteorol Soc 148(749):3604–3621. https://doi.org/10.1002/qj.4376
Stiperski I, Calaf M (2018) Dependence of near-surface similarity scaling on the anisotropy of atmospheric turbulence. Q J R Meteorol Soc 144(712):641–657. https://doi.org/10.1002/qj.3224
Stopa JE, Wang C, Vandemark D, Foster R, Mouche A, Chapron B (2022) Automated global classification of surface layer stratification using high-resolution sea surface roughness measurements by satellite synthetic aperture radar. Geophys Res Lett 49(12):1–11. https://doi.org/10.1029/2022GL098686
Stull RB (1988) An introduction to boundary layer meteorology. Atmospheric Sciences Library, Kluwer Academic Publishers, Dordrecht, Boston
Townsend AA (1976) The structure of turbulent shear flow, 2nd edn. Cambridge University Press, Cambridge
Van de Wiel BJH, Moene AF, De Ronde WH, Jonker HJJ (2008) Local similarity in the stable boundary layer and mixing-length approaches: consistency of concepts. Boundary-Layer Meteorol 128(1):103–116. https://doi.org/10.1007/s10546-008-9277-y
Van de Wiel BJH, Moene AF, Jonker HJJ (2012) The cessation of continuous turbulence as precursor of the very stable nocturnal boundary layer. J Atmos Sci 69(11):3097–3115. https://doi.org/10.1175/JAS-D-12-064.1
Van de Wiel BJH, Moene AF, Jonker HJJ, Baas P, Basu S, Donda JMM, Sun J, AaM Holtslag (2012) The minimum wind speed for sustainable turbulence in the nocturnal boundary layer. J Atmos Sci 69(11):3116–3127. https://doi.org/10.1175/JAS-D-12-0107.1
Van der Linden S, Van de Wiel BJH, Petenko I, Van Heerwaarden CC, Baas P, Jonker HJJ (2020) A Businger mechanism for intermittent bursting in the stable boundary layer. J Atmos Sci 77(10):3343–3360. https://doi.org/10.1175/JAS-D-19-0309.1
Venayagamoorthy SK, Stretch DD (2010) On the turbulent Prandtl number in homogeneous stably stratified turbulence. J Fluid Mech 644:359–369. https://doi.org/10.1017/S002211200999293X
Vercauteren N, Boyko V, Faranda D, Stiperski I (2019) Scale interactions and anisotropy in stable boundary layers. Q J R Meteorol Soc 145(722):1799–1813. https://doi.org/10.1002/qj.3524
Watanabe T, Riley JJ, Nagata K, Matsuda K, Onishi R (2019) Hairpin vortices and highly elongated flow structures in a stably stratified shear layer. J Fluid Mech 878:37–61. https://doi.org/10.1017/jfm.2019.577
Weber RO, Kaufmann P (1998) Relationship of synoptic winds and complex terrain flows during the MISTRAL field experiment. J Appl Meteorol Climatol 37(11):1486–1496. https://doi.org/10.1175/1520-0450(1998)037%3C1486:ROSWAC%3E2.0.CO;2
Whiteman CD, Doran JC (1993) The relationship between overlying synoptic-scale flows and winds within a valley. J Appl Meteorol Climatol 32(11):1669–1682. https://doi.org/10.1175/1520-0450(1993)032%3C1669:TRBOSS%3E2.0.CO;2

Williamson JH (1980) Low-storage Runge–Kutta schemes. J Comput Phys 35(1):48–56. https://doi.org/10.1016/0021-9991(80)90033-9

Wippermann F, Gross G (1981) Construction of orographically influenced wind roses for given distributions of the large-scale wind. Contrib Atmos Phys (Germany, Federal Republic of) 54:4

Wyngaard JC (1973) On surface layer turbulence. In: Haugen DH (ed) Workshop on Micrometeorology, Ed., American Meteorological Society, p 392

Yagüe C, Maqueda G, Rees JM (2001) Characteristics of turbulence in the lower atmosphere at Halley IV station, Antarctica. Dyn Atmos Oceans 34(2):205–223. https://doi.org/10.1016/S0377-0265(01)00068-9

Yakhot V, Orszag SA (1986) Renormalization group analysis of turbulence. I. Basic theory. J Sci Comput 1(1):3–51. https://doi.org/10.1007/BF01061452

Zilitinkevich SS, Elperin T, Kleeorin N, Rogachevskii I, Esau I, Mauritsen T, Miles MW (2008) Turbulence energetics in stably stratified geophysical flows: strong and weak mixing regimes. Q J R Meteorol Soc 134(633):793–799. https://doi.org/10.1002/qj.264

Zilitinkevich SS, Tyuryakov SA, Troitskaya YuI, Mareev EA (2012) Theoretical models of the height of the atmospheric boundary layer and turbulent entrainment at its upper boundary. Izv Atmos Ocean Phys 48(1):133–142. https://doi.org/10.1134/S0001433812010148